

MULTIPLE WAVE SOLUTIONS IN A DIFFUSIVE PREDATOR-PREY MODEL WITH STRONG ALLEE EFFECT ON PREY AND RATIO-DEPENDENT FUNCTIONAL RESPONSE

EDGARDO VILLAR-SEPÚLVEDA*, PABLO AGUIRRE*, AND VÍCTOR F. BREÑA-MEDINA†

ABSTRACT. A thorough analysis is performed in a predator-prey reaction-diffusion model which includes three relevant complex dynamical ingredients: (a) a strong Allee effect; (b) ratio-dependent functional responses; and (c) transport attributes given by a diffusion process. As is well-known in the specialized literature, these aspects capture adverse survival conditions for the prey, predation search features and non-homogeneous spatial dynamical distribution of both populations. We look for traveling-wave solutions and provide rigorous results coming from a standard local analysis, numerical bifurcation analysis, and relevant computations of invariant manifolds to exhibit homoclinic and heteroclinic connections and periodic orbits in the associated dynamical system in \mathbb{R}^4 . In so doing, we present and describe a diverse zoo of traveling wave solutions; and we relate their occurrence to the Allee effect, the spreading rates and propagation speed. In addition, homoclinic chaos is manifested via both saddle-focus and focus-focus bifurcations as well as a Belyakov point. An actual computation of global invariant manifolds near a focus-focus homoclinic bifurcation is also presented to unravel a multiplicity of wave solutions in the model. A deep understanding of such ecological dynamics is therefore highlighted.

1. INTRODUCTION

One of the main objectives of ecology is to understand the interactions of individual organisms with those of the same species and with other actors in their environment, and how populations distribute when forming communities. In particular, predation —and its associated mathematical models— has been part of the dominant topics in ecology from the beginning of this discipline [12, 51]. Since the early works of Volterra [62] onwards, predator-prey models have been continuously studied by mathematicians and biologists thanks to their adequate generalization of practical scenarios and for being an essential guide in biological populations. In all these cases, predator-prey models may shed light on necessary conditions for species to coexist and not to be doomed to extinction [12, 51].

In this work, we are interested in the interaction between predator and prey when this is driven by spatial distribution and propagation features —related to a transport process that favors food searching events—, and the critical densities that the prey population must achieve in order to survive in the long term. The starting point of our work is the following Gause type deterministic predator-prey model first studied in [4]:

$$\begin{cases} \frac{dN}{dt} = rN \left(1 - \frac{N}{K}\right) \left(\frac{N}{M} - 1\right) - \frac{aNP}{P + ahN}; \\ \frac{dP}{dt} = e \frac{aNP}{P + ahN} - qP. \end{cases} \quad (1)$$

2020 *Mathematics Subject Classification.* 37N25, 35C07, 92D40, 37C29, 37D10, 37G20, 35Q92.

Key words and phrases. Homoclinic and heteroclinic orbits, traveling waves, invariant manifolds, bifurcation analysis, Allee effect.

EVS was partially funded by Programa de Incentivo a la Iniciación Científica PIIC DGIIP-UTFSM. EVS and PA were partially funded by Proyecto Interno UTFSM PI-LI-19-06. PA also thanks Proyecto Basal CMM Universidad de Chile. VFBM thanks the financial support by Asociación Mexicana de Cultura A.C..

Here $N = N(t)$ and $P = P(t)$ are functions of time that represent the population sizes of prey and predators, respectively, provided that $P + ahN > 0$. The main ingredients of (1) are a strong Allee effect on prey and a ratio-dependent functional response. Let us give a brief overview of these two features. The Allee effect [56] is a phenomenon that may affect a species at low population densities, sometimes even related to the emergence of extinction risks. At low densities, predators can induce a phenomenon called the *Allee effect by predation* affecting the prey species [28, 30]. Under these unfavorable conditions, some species can have difficulties defending themselves from predators, hiding or taking anti-predation measures when their population density is low [64, 66]. Another manifestation of the Allee effect is the difficulty of a species to use cooperation and aggregation tactics in other strategic activities such as food searching, to resist unfavorable environmental conditions, or to find mating partners. Hence, while at a low population density, each individual may take advantage of a higher amount of resources, sometimes this benefit is not as significant as the losses associated with its small density. The study of the Allee effect can have a massive impact on the dynamics of populations of many plants and animals [20]. According to the literature, a species can be affected by two main types of Allee effect. The strong Allee effect is characterized by the presence of a threshold (known as the *Allee threshold*). Below this threshold, the population density growth becomes negative, so that the population becomes prone to extinction [20]. In model (1) we assume that the prey is affected by a strong Allee effect. This is manifested in the presence of parameter M . Indeed, in the absence of predators, if the prey population is below the threshold M , we have $dN/dt < 0$ and, hence, this species tends to extinction in the long term. Since Allee effect is a phenomenon occurring typically at low population densities, we consider $0 < M \ll K$, where K is the carrying capacity of the prey. On the other hand, the so-called weak Allee effect describes a scenario in which low-level populations show a reduced (but positive) per capita growth rate [20]. Hence, a subtle relevant distinction between these two density-dependent growth rates lies on the fact that the strong Allee effect captures whether a population critical size is reached. In other words, if the prey population size is exactly the Allee-threshold parameter value, the prey growth will only be dependent on interaction, as in (1) for instance, with the predators.

Since the Allee effect is related to population extinction, an understanding of this phenomenon is very relevant for ecological administration and conservation [56]. Many studies have been carried out in this regard, as can be seen in [4, 18, 21, 56]. Different models have shown that the Allee effect increases the risk of population extinction as the Allee threshold rises [56]. When predator-prey interaction is present —as is the case in (1)—, this imposes a two-dimensional state space for the variables x and y . In such case, the Allee threshold is typically a one-dimensional object in the (x, y) -plane. Recent findings reveal that this threshold can be the basin boundary of a positive (coexistence) equilibrium, or a limit cycle, or a homoclinic orbit [4, 18].

The second feature in (1) is a ratio-dependent functional response. The motivation for this comes from two well-known paradoxes in Gause type predator-prey models. First, enriching a predator-prey system causes an increase in the equilibrium density of the predator but not in that of the prey, destabilizing the community equilibrium; this is known as the paradox of enrichment [57, 42]. Also, in Gause type models there can not exist a stable low prey density equilibrium, also known as the biological control paradox [14, 48]. One way to deal with these paradoxes is by considering ratio-dependent functional responses [42]. A generic ratio-dependent functional response depends on the population density ratio between prey and predators N/P . Some examples of ratio-dependent functional responses can be formulated by the direct substitution $N \mapsto N/P$ in the classic Holling family of functional responses [22, 36, 37, 61]. In particular, in (1), prey consumption by predators follows a modified Holling II ratio-dependent functional response. Here, $e > 0$ is the conversion efficiency of the predator, $h > 0$ is the predator handling time, and $a > 0$ is the maximum per capita

consumption rate of predators. The remaining parameters in (1) are the prey population natural intrinsic growth rate $r > 0$, and the predator natural mortality rate $q > 0$.

To consider a ratio-dependent functional response has a number of additional advantages. According to animal ecologists, ratio-dependent models are more suitable for predator-prey interactions where predation involves a searching process [11, 34, 42]. Moreover, the empirical evidence suggests that the ratio-dependent modelling approach produces more realistic dynamics from a biological point of view [8, 10, 14].

Model (1) presents the technical difficulty of not being well-defined at the origin $(N, P) = (0, 0)$. A usual technique to deal with this problem is to continuously extend the system to one which is well defined at this point [4, 5, 6, 29]. This can be achieved by applying the following transformation and defining new parameters:

$$(u, v, \tau) := \left(\frac{N}{K}, \frac{P}{ahK}, \frac{rK(1+ah)}{M(P+ahN)}t \right), \quad (\alpha, \beta, \gamma, m) := \left(\frac{aM}{rK}, \frac{eM}{rhK}, \frac{qM}{rK}, \frac{M}{K} \right).$$

In this way we obtain

$$\begin{cases} \frac{du}{dt} = u(u-m)(1-u)(u+v) - \alpha uv, \\ \frac{dv}{dt} = \beta uv - \gamma v(u+v), \end{cases} \quad (2)$$

where $u = u(t)$ and $v = v(t)$ represent rescaled population sizes of prey and predators, respectively, and we have renamed $\tau \mapsto t$ once again for notation convenience. System (2) represents a \mathcal{C}^∞ -qualitatively equivalent polynomial extension of (1): it is \mathcal{C}^∞ -qualitatively equivalent to (1) whenever $(P, N) \neq (0, 0)$ and, it is well-defined at the origin. In [4], the authors sought to explain the consequences of the (dis)appearance of limit cycles, homoclinic orbits, and heteroclinic connections in the global arrangement of the phase plane near a Bogdanov-Takens bifurcation. In particular, they point out that the Allee threshold in the two-dimensional system is given as the boundary of the basin of attraction of an attracting positive equilibrium, and they determine conditions for mutual extinction or survival of the populations.

On the other hand, the spatial component of ecological interactions has been identified as a significant factor in the behavior of communities [31, 50, 51]. For instance, breaking symmetry features are usually found in ratio-dependent models that take into account certain heterogeneous spatial population distributions, (see e.g. [9]). We consider that even though individuals may follow a simple random motion, the population however may behave as a whole in a deterministic way. Such a property yields to a transport process that can be understood from a mean-field viewpoint; that is, the population transport dynamics is captured by the Fokker-Planck equation, which in the simplest version particularly accounts for a standard diffusion process; see [52, 53]. Recent studies have considered different spatial phenomena in population dynamics, such as propagation and migration [17, 44]. These have led to obtaining a solid argument that highlights the relevance of their study by finding traveling wave solutions that move in space, preserving their shape as time passes [46, 47, 59]. This kind of solutions emerges as a suitable mathematical approach to describe wave-like spatial movement of populations. Evidence of this type of behavior has been found in several models used to model pest outbreaks, chemical concentration, colonization of a space region by a population, spatial dispersal of epidemics, etc.; see, for instance, the textbooks [50, 51] and the references therein. Typically, traveling waves represent spatiotemporal transitions from one homogeneous steady state to another one, or to itself; see [38, 46, 51, 65]. Moreover, recent evidence indicates that multi-year periodic traveling waves can also be found [59]. Following this motivation, we consider an extension of (2) by taking into account a diffusion transport process on both populations. In so doing, we obtain the following reaction-diffusion

system:

$$\begin{cases} u_t = D_1 u_{xx} + u(u - m)(1 - u)(u + v) - \alpha uv, \\ v_t = D_2 v_{xx} + \beta uv - \gamma v(u + v), \end{cases} \quad (3)$$

where partial derivatives short notation is used: $w_t = \partial w / \partial t$ and $w_{xx} = \partial^2 w / \partial x^2$. In (3), $x \in [-L, L]$ is the spatial variable and the characteristic length of the predator-prey interaction domain is assumed to be such that $L \rightarrow \infty$ as this sort of solutions are known to arise in systems as (3) (see e.g. [15, 49, 45]); $t > 0$ remains the temporal independent variable, and diffusion rates $D_1, D_2 > 0$ correspond to population mobilities which are a measure of the spatial dispersion efficiency of prey and predators, respectively [51].

Typically, the mathematical analysis to find traveling wave solutions involves the reduction of the reaction-diffusion equations into a system of ordinary differential equations in which one searches for heteroclinic or homoclinic orbits. However, the problem of obtaining these connecting orbits and associated global (un)stable manifolds is a challenging task. Moreover, the type of solutions are determined by the geometry of the spatial domain and whether boundary conditions in system (3) are Neumann, Dirichlet or periodic. Nonetheless, with the exception of a few concrete examples (see, e.g., [38]), in general, there are no analytical expressions for homoclinic orbits or nonlocal normal forms. Hence, it is frequent to make use of reductions to Poincaré maps in suitable cross sections or numerical techniques to obtain them; see [60, 67] as examples of this kind of analysis in the context of insect dispersal. Today, homoclinic and heteroclinic orbits can readily be computed and continued with software packages like AUTO [25] (with its extension HOMCONT [16]) and MATCONT [23] with high accuracy. In addition, one can locate homoclinic and heteroclinic connections as intersections of global invariant manifolds. This can be achieved by direct computation and inspection of the manifolds [2, 7] or by setting additional techniques such as Lin's method [39]. While one-dimensional invariant manifolds can be approximated using straightforward integration from a given initial condition, the computation of higher-dimensional manifolds of equilibria and periodic orbits requires advanced numerical techniques; see for example [1, 32, 40, 41]. Moreover, while some works have dealt with traveling waves associated with three-dimensional vector fields in population models [47, 60, 67], our problem involves a four-dimensional phase space, which is as a major challenge. Although the human brain is efficient when capturing depth in flat images of 3-dimensional objects, this ability is not as effective in higher dimensions [19, 54]. When trying to visualize objects in a 4D phase space—such as invariant manifolds—, standard projections may give rise to false intersections between them. These artifacts due to projections must be detected and differentiated from real intersections to ensure or discard the existence of homoclinic or heteroclinic connections. To do so, we make extensive use of dynamical systems theory and topological arguments to justify our findings.

With a strategic combination of invariant manifold analysis and bifurcation theory we find the traveling wave solutions identifying each of them as a specific heteroclinic/homoclinic connection or a periodic orbit in the four-dimensional phase space. We classify these solutions into 12 different classes depending on the topological type of the associated orbit. We also determine conditions on the model parameters so that there is such a particular kind of solution and identify homoclinic chaotic dynamics as one of the sources of complicated behaviour. All in all, this collection of dynamical objects represent desired wave fronts, wave pulses and wave trains, corresponding to bounded solutions of (3) which ensure survival of both populations in the long term.

This paper is organized as follows: section 2 presents some preliminary results and background. Local analysis near steady states is included in section 3, while the bifurcation analysis is presented in section 4. Wave pulses, wave trains and wave fronts are discussed in sections 5, 6 and 7, respectively. Section 8 presents a description of the multiple wave fronts found near a focus-focus homoclinic bifurcation. Section 9 discussed the influence of the propagation speed and the diffusion ratio on the

occurrence of the different wave pulses. Section 10 analyzes the existence of traveling fronts for the prey population in the absence of predators. Finally, section 11 presents a summary and discussion of the main results. In addition, in the Appendix A, we briefly review the method we used to obtain the global two-dimensional manifolds.

2. MODEL REDUCTION, DEFINITIONS AND NOTATION

For future convenience, the first step to study traveling wave solutions in (3) is to make a time rescaling and a change of parameters given, respectively, by

$$(4) \quad t \rightarrow D_2 t, \quad (d, s, b, g, a, m) = \left(\frac{D_1}{D_2}, \frac{1}{D_2}, s\beta, s\gamma, s\alpha, m \right) \in \mathbb{R}_+^5 \times]0, 1[.$$

Thus, we can write system (3), equivalently, as

$$(5) \quad \begin{cases} u_t = du_{xx} + su(u-m)(1-u)(u+v) - auv; \\ v_t = v_{xx} + buv - gv(u+v). \end{cases}$$

Here, $d = D_1/D_2$ represents the ratio of diffusion rates of prey and predators, respectively, and appears as an explicit parameter in (5). If $d > 1$ (resp. $d < 1$), prey individuals are more (resp. less) efficient to disperse in space compared to the predators.

We now consider the so-called wave variable $z := x + ct$, where $c > 0$ is the wave speed and we look for solutions of (5) of the form $U(z) = u(x, t)$, $V(z) = v(x, t)$. Applying the chain rule and substituting this into (5), we obtain the following set of second order ordinary differential equations

$$(6) \quad \begin{cases} c \frac{dU}{dz} = d \frac{d^2U}{dz^2} + sU(U-m)(1-U)(U+V) - aUV; \\ c \frac{dV}{dz} = \frac{d^2V}{dz^2} + bUV - gV(U+V). \end{cases}$$

Naming the auxiliary variables $W = dU/dz$ and $R = dV/dz$, system (6) can be expressed equivalently as the vector field

$$(7) \quad X : \begin{cases} \frac{dU}{dz} = W, \\ \frac{dV}{dz} = R, \\ \frac{dW}{dz} = \frac{1}{d} (cW - sU(U-m)(1-U)(U+V) + aUV), \\ \frac{dR}{dz} = cR - bUV + gV(U+V). \end{cases}$$

The biologically relevant region of the four-dimensional phase space of (7) is the set $\Omega = \{(U, V, W, R) \in \mathbb{R}^4 : U \geq 0, V \geq 0\}$. A traveling wave of (5) is any bounded solution of the system (7) contained in the realistic domain Ω . These solutions are functions that “travel” in space, preserving their form as time goes by. A sketch of a traveling wave moving to the left with speed $c > 0$ as time increases is depicted in figure 1.

As we need to find bounded solutions of the system (7), we focus our attention on three special types of traveling waves: wave pulses, wave fronts, and wave trains [38]. Typically, pulses and fronts are associated with homoclinic and heteroclinic orbits, respectively, in the reduced ODE system (such as (7)). In turn, wave trains correspond to periodic orbits of the associated ODE system.

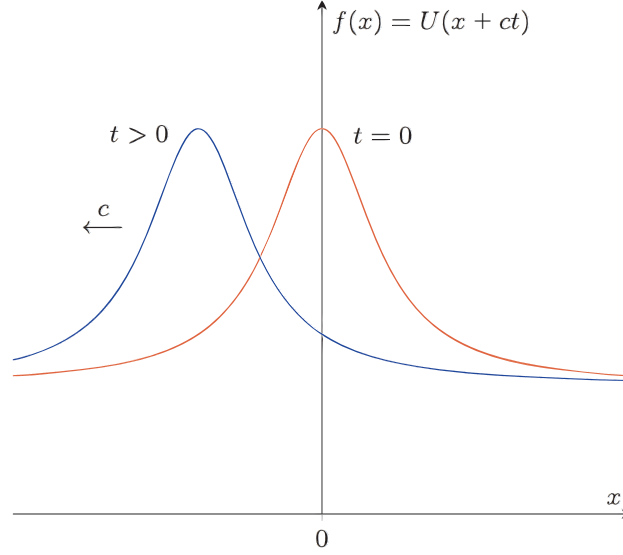


FIGURE 1. Sketch of the spatial propagation of a traveling wave solution, with $c > 0$.

2.1. Pulses and fronts as homoclinic and heteroclinic orbits. An orbit of the vector field (7) is called *homoclinic* if it connects an equilibrium to itself converging to this point as the orbit parameter $z \rightarrow \pm\infty$. Figure 2(a) shows an actual homoclinic orbit of (7) found with the method presented later in section 5. The homoclinic orbit connects the equilibrium point $\mathbf{q} = (q_u, q_v, 0, 0)$ (given explicitly in section 3) to itself. The time series of U and V associated with this connecting orbit are shown in figure 2(b) in blue and orange, respectively. The profile of this solution is characterized by a large deviation (or pulse) in the amplitudes of U and V followed by a convergence back to the resting state. This corresponds to a wave pulse in the original system (5) that travels from a spatially homogeneous stationary solution to itself. Therefore, homoclinic orbits of (7) correspond to wave pulses of (5). Formally, this wave pulse satisfies for all $x \in \mathbb{R}$ in (5), and respectively in (7), that

$$(8) \quad \lim_{t \rightarrow \pm\infty} (u(t, x), v(t, x)) = (q_u, q_v) \Leftrightarrow \lim_{z \rightarrow \pm\infty} (U(z), V(z), W(z), R(z)) = \mathbf{q}.$$

On the other hand, an orbit is said to be *heteroclinic* if it converges to different equilibria at each end $z \rightarrow \infty$ or $z \rightarrow -\infty$. Heteroclinic orbits of (7) correspond to wave fronts of (5). Figure 3(a) shows a heteroclinic orbit connecting equilibrium \mathbf{q} to equilibrium $\mathbf{p} = (p_u, p_v, 0, 0)$ (given explicitly below in section 3). This corresponds to a wave of (5) that makes the transition from one spatially homogeneous stationary solution to another as is shown in figure 3(b). Formally, this wave front satisfies

$$\begin{aligned} & \left. \begin{aligned} \lim_{t \rightarrow -\infty} (u(t, x), v(t, x)) &= (q_u, q_v), & \forall x \in \mathbb{R}, \\ \lim_{t \rightarrow +\infty} (u(t, x), v(t, x)) &= (p_u, p_v), & \forall x \in \mathbb{R}, \end{aligned} \right\} \text{in (5)} \\ \Leftrightarrow & \left. \begin{aligned} \lim_{z \rightarrow -\infty} (U(z), V(z), W(z), R(z)) &= \mathbf{q}, \\ \lim_{z \rightarrow +\infty} (U(z), V(z), W(z), R(z)) &= \mathbf{p}, \end{aligned} \right\} \text{in (7)}. \end{aligned} \quad (9)$$

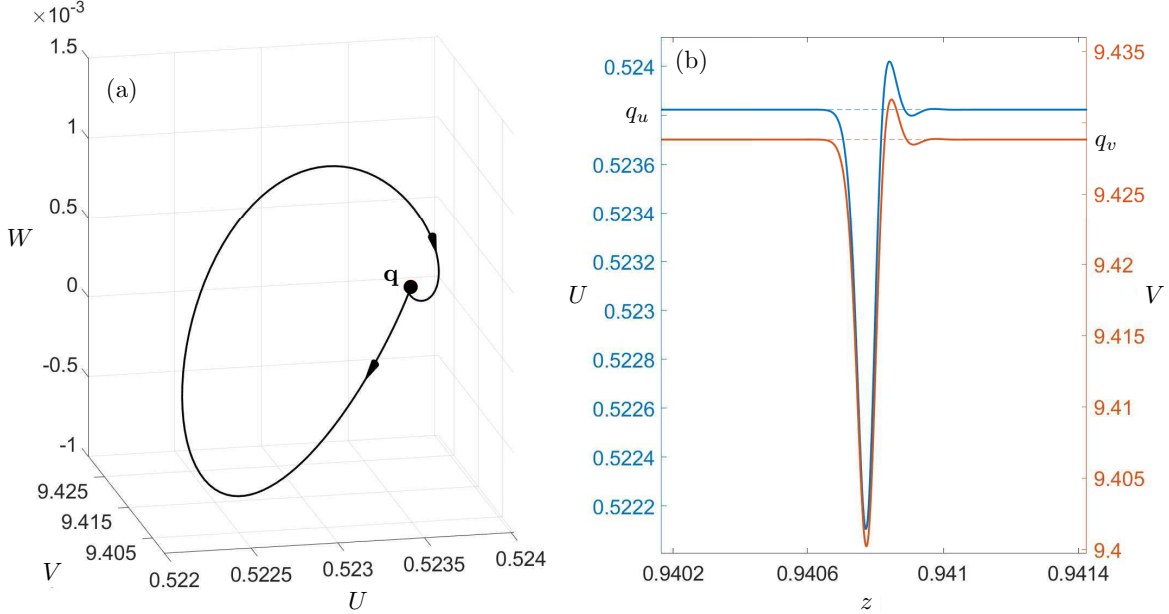


FIGURE 2. Profile of a wave pulse. Panel (a) shows a homoclinic orbit which joins the equilibrium \mathbf{q} to itself in the long term, projected onto the UVW space, while panel (b) shows the time series of U and V associated with this solution in blue and orange, respectively; here, the range of z values in the horizontal axis is restricted to the interval where the variables U and V develop the pulse. Parameter values are $a = 24$, $b = 19$, $g = 1$, $c = 1$, $s = 100$, $m = 0.0463358$, and $d = 1.3080156$.

From (8) and (9), the homoclinic and heteroclinic orbits (and their associated time series) as solutions of (7) are parameterized by $z \in]-\infty, \infty[$. However, for computational procedures, this independent variable is rescaled to $z \in]0, 1[$ in all our results; see the Appendix A for more details. Moreover, in figure 2 (and for every other wave pulse shown throughout this paper) we restrict the values of z to those compact subintervals of $]0, 1[$ where the pulses are easier to see.

2.2. Wave trains and periodic orbits. The third kind of wave solution of (5) we are interested in is wave trains. These solutions correspond to periodic orbits of system (7), as is illustrated in figure 4. A cycle of (7) is associated with a traveling wave of (5) with a periodic profile in both space and time. More formally, for every periodic orbit in the domain Ω of (7) there exists $T > 0$ (called the *period*) such that

$$(10) \quad \begin{aligned} & (u(\hat{x}, \hat{t}), v(\hat{x}, \hat{t})) = (u(x, t), v(x, t)) \text{ in (5),} \\ & \Leftrightarrow \\ & (U(\hat{z}), V(\hat{z}), W(\hat{z}), R(\hat{z})) = (U(z), V(z), W(z), R(z)) \text{ in (7),} \end{aligned}$$

where $\hat{x} = x + \alpha T$, $\hat{t} = t + \frac{(1-\alpha)}{c}T$, $\hat{z} = z + T$, and $\alpha \in [0, 1]$.

For computational purposes, the period of every periodic orbit of (7) is rescaled to $T = 1$; see the Appendix A. In particular, in figure 4 (and for every other wave train shown throughout this paper) we restrict the values of z to one such period of the cycle.

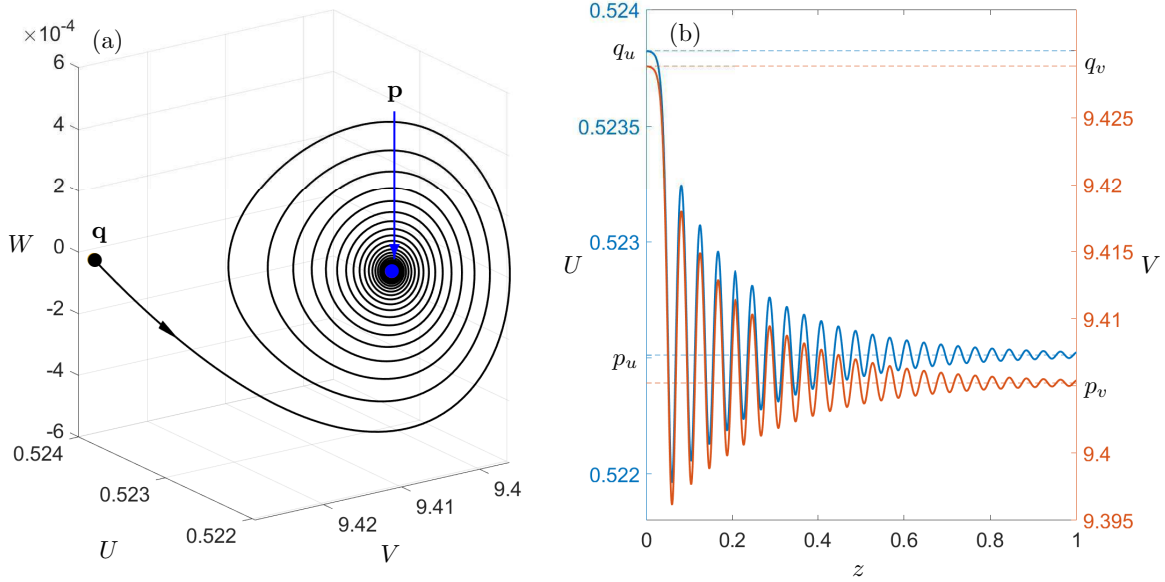


FIGURE 3. Profile of a wave front. Panel (a) shows a heteroclinic orbit from \mathbf{q} to \mathbf{p} , projected onto the UVW space, while panel (b) shows the time series of U and V associated with the same solution. Parameter values are the same as in figure 2 except for $d = 2.2883206$, and $c = 0.4372925$.

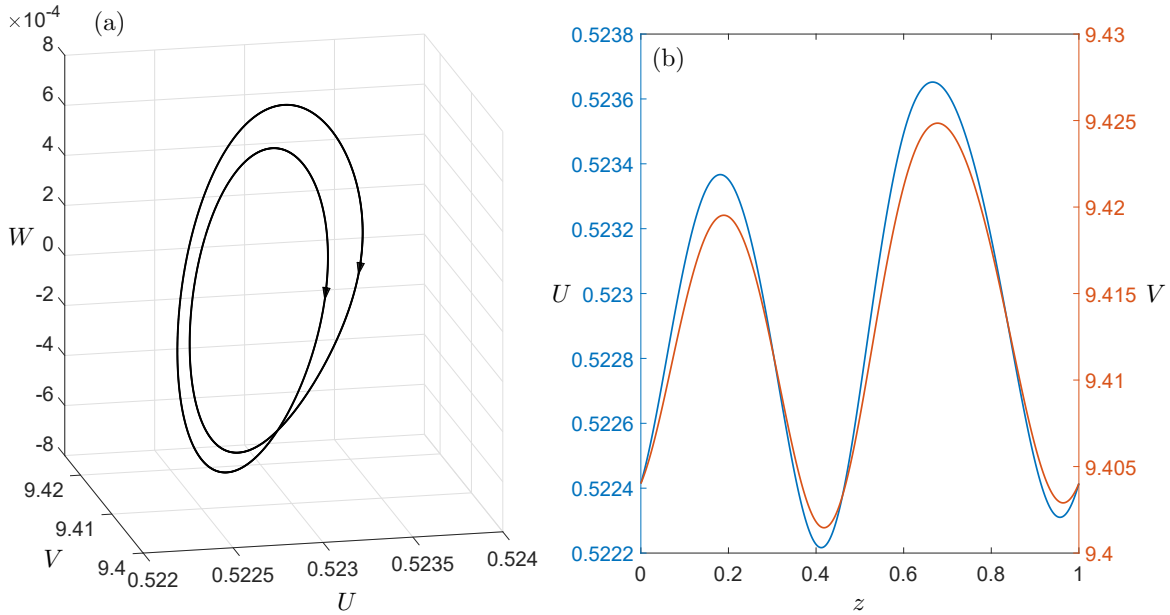


FIGURE 4. Profile of a wave train. Panel (a) shows a periodic orbit projected onto the UVW space, while panel (b) shows the time series of U and V contained in a (rescaled) period of length 1. Parameter values are the same as in figure 2 except for $d = 1.3107$.

2.3. Invariant manifolds. Homoclinic and heteroclinic orbits in ordinary differential equations — such as (7) — are intersections of invariant manifolds of equilibria. If all the eigenvalues of the associated Jacobian matrix at an equilibrium, say \mathbf{x}^* , have non-zero real part, we say that \mathbf{x}^* is *hyperbolic*; otherwise, it is called *non-hyperbolic*. In the hyperbolic case, if all the eigenvalues have negative (resp. positive) real part, the equilibrium is called an *attractor* (resp. *repeller*). If \mathbf{x}^* has eigenvalues with positive and negative real parts, the equilibrium is a *saddle*. In such case, the stable manifold theorem [33, 43] ensures the existence of the *local stable and unstable manifolds* of \mathbf{x}^* defined, respectively, as

$$W_{\text{loc}}^s(\mathbf{x}^*) = \{y \in N : \varphi^z(y) \rightarrow \mathbf{x}^* \text{ when } z \rightarrow \infty, \text{ and } \varphi^z(y) \in N, \forall z \geq 0\},$$

$$W_{\text{loc}}^u(\mathbf{x}^*) = \{y \in N : \varphi^z(y) \rightarrow \mathbf{x}^* \text{ when } z \rightarrow -\infty, \text{ and } \varphi^z(y) \in N, \forall z \leq 0\},$$

where N is a neighborhood of \mathbf{x}^* . In our particular case, φ^z is the flow of the vector field (7), where the orbits are parameterized by the independent variable z . The sets $W_{\text{loc}}^s(\mathbf{x}^*)$ and $W_{\text{loc}}^u(\mathbf{x}^*)$ are immersed, smooth manifolds tangent at \mathbf{x}^* to the eigenspaces $E^s(\mathbf{x}^*)$ and $E^u(\mathbf{x}^*)$, respectively. Moreover, the dimension of $W_{\text{loc}}^s(\mathbf{x}^*)$ (resp. $W_{\text{loc}}^u(\mathbf{x}^*)$) is the same as that of $E^s(\mathbf{x}^*)$ (resp. $E^u(\mathbf{x}^*)$). That is, $\dim W_{\text{loc}}^s(\mathbf{x}^*)$ (resp. $\dim W_{\text{loc}}^u(\mathbf{x}^*)$) is the number of eigenvalues with negative (resp. positive) real part. By extending $W_{\text{loc}}^s(\mathbf{x}^*)$ and $W_{\text{loc}}^u(\mathbf{x}^*)$ by the flow φ^z we obtain the *global stable and unstable manifolds* given, respectively, by

$$W^s(\mathbf{x}^*) = \{y \in \mathbb{R}^4 : \varphi^z(y) \rightarrow \mathbf{x}^* \text{ as } z \rightarrow \infty\},$$

$$W^u(\mathbf{x}^*) = \{y \in \mathbb{R}^4 : \varphi^z(y) \rightarrow \mathbf{x}^* \text{ as } z \rightarrow -\infty\}.$$

In the example of figure 2, the homoclinic connection is an orbit in $W^u(\mathbf{q})$ which comes back to \mathbf{q} along the stable manifold $W^s(\mathbf{q})$, i.e., it is in the intersection $W^u(\mathbf{q}) \cap W^s(\mathbf{q})$. Furthermore, in figure 3, the heteroclinic connection is an orbit in $W^u(\mathbf{q})$ which moves away from \mathbf{q} , but it is also contained in $W^s(\mathbf{p})$ and, hence, heads toward \mathbf{p} . That is, this heteroclinic orbit lies in $W^u(\mathbf{q}) \cap W^s(\mathbf{p})$.

On the other hand, if \mathbf{x}^* is a non-hyperbolic equilibrium, there is a locally invariant manifold, denoted as $W^c(\mathbf{x}^*)$, and known as the *center manifold*. The manifold $W^c(\mathbf{x}^*)$ is tangent at \mathbf{x}^* to the eigenspace $E^c(\mathbf{x}^*)$ and $\dim W^c(\mathbf{x}^*) = \dim E^c(\mathbf{x}^*)$, and captures the essential long term dynamics in a neighbourhood of \mathbf{x}^* ; we refer to [33] for more details.

3. LOCAL ANALYSIS

System (7) has at most five equilibrium points in the domain Ω , which are given by $\mathbf{p}_0 = (0, 0, 0, 0)$, $\mathbf{p}_m = (m, 0, 0, 0)$, $\mathbf{p}_1 = (1, 0, 0, 0)$, $\mathbf{p} = (p_u, p_v, 0, 0)$, and $\mathbf{q} = (q_u, q_v, 0, 0)$, where

$$(11a) \quad q_u = \frac{bs(1+m) + \sqrt{bs\Delta}}{2bs}, \quad (11c) \quad p_u = \frac{bs(1+m) - \sqrt{bs\Delta}}{2bs},$$

$$(11b) \quad q_v = \frac{(b-g)}{g}q_u, \quad (11d) \quad p_v = \frac{(b-g)}{g}p_u,$$

provided $\Delta = bs(m-1)^2 - 4a(b-g) \geq 0$ and $q_u, q_v, p_u, p_v \geq 0$. Under these conditions, we have the following result on the stability of \mathbf{p}_0 , \mathbf{p}_m and \mathbf{p}_1 :

Proposition 1. *Let us consider the quantities*

$$\Delta_m^1 := c^2 + 4(g-b)m, \quad \Delta_m^2 := c^2 - 4d(1-m)m^2s.$$

Then, system (7) satisfies the following statements:

- (1) \mathbf{p}_0 is an unstable non-hyperbolic equilibrium, with $\dim(W^u(\mathbf{p}_0)) = 2$ and $\dim(W^c(\mathbf{p}_0)) = 2$.
- (2) If $b < g$, then \mathbf{p}_m and \mathbf{p}_1 are hyperbolic saddles, with $\dim(W^s(\mathbf{p}_m)) = 1$, $\dim(W^u(\mathbf{p}_m)) = 3$, $\dim(W^s(\mathbf{p}_1)) = 2$ and $\dim(W^u(\mathbf{p}_1)) = 2$.

(3) If $b > g$, then \mathbf{p}_m is a hyperbolic repeller and \mathbf{p}_1 is a hyperbolic saddle with $\dim(W^s(\mathbf{p}_1)) = 1$ and $\dim(W^u(\mathbf{p}_1)) = 3$. In addition, if $\Delta_m^1 > 0$ and $\Delta_m^2 > 0$, then \mathbf{p}_m is a repelling node.

Proof. If we denote the vector field (7) as X , its Jacobian matrix evaluated at the points \mathbf{p}_0 , \mathbf{p}_m and \mathbf{p}_1 is given, respectively, by:

$$DX(\mathbf{p}_0) = \begin{pmatrix} 0 & 0 & 1 & 0 \\ 0 & 0 & 0 & 1 \\ 0 & 0 & \frac{c}{d} & 0 \\ 0 & 0 & 0 & c \end{pmatrix}, \quad DX(\mathbf{p}_m) = \begin{pmatrix} 0 & 0 & 1 & 0 \\ 0 & 0 & 0 & 1 \\ -\frac{(1-m)m^2s}{d} & \frac{am}{d} & \frac{c}{d} & 0 \\ 0 & (g-b)m & 0 & c \end{pmatrix},$$

$$\text{and } DX(\mathbf{p}_1) = \begin{pmatrix} 0 & 0 & 1 & 0 \\ 0 & 0 & 0 & 1 \\ \frac{(1-m)s}{d} & \frac{a}{d} & \frac{c}{d} & 0 \\ 0 & g-b & 0 & c \end{pmatrix}.$$

Denoting by λ_i^j the i -th eigenvalue of the equilibrium \mathbf{p}_j , $j \in \{0, 1, m\}$, then we see that

$$\begin{cases} \lambda_{1,2}^0 = 0, \\ \lambda_3^0 = \frac{c}{d} > 0, \\ \lambda_4^0 = c > 0. \end{cases} \quad \begin{cases} \lambda_{1,2}^m = \frac{c \pm \sqrt{\Delta_m^1}}{2}, \\ \lambda_{3,4}^m = \frac{c \pm \sqrt{\Delta_m^2}}{2d}, \end{cases} \quad \begin{cases} \lambda_{1,2}^1 = \frac{c \pm \sqrt{c^2 + 4(g-b)}}{2}, \\ \lambda_{3,4}^1 = \frac{c \pm \sqrt{c^2 + 4d(1-m)s}}{2d}. \end{cases}$$

Since $DX(\mathbf{p}_0)$ has two zero and two positive eigenvalues, then \mathbf{p}_0 is an unstable non-hyperbolic equilibrium. The remaining statements are direct consequences of the Hartman-Grobman theorem [33] and the stable manifold theorem. As for \mathbf{p}_m , since $0 < m < 1$, then $\Delta_m^2 = c^2 - 4d(1-m)m^2s < c^2$. Furthermore, if $b < g$, then $\Delta_m^1 = c^2 + 4(g-b)m > c^2$. Thus we have that

$$\lambda_1^m = \frac{c + \sqrt{\Delta_m^1}}{2} > 0, \quad \lambda_2^m = \frac{c - \sqrt{\Delta_m^1}}{2} < 0, \quad \text{Re}(\lambda_{3,4}^m) > 0,$$

which implies the desired result. On the other hand, if $b > g$, then $\Delta_m^1 < c^2$, which implies that $\lambda_2^m > 0$. In the particular case that $b > g$, $\Delta_m^1 > 0$ and $\Delta_m^2 > 0$, the eigenvalues $\lambda_{3,4}^m$ of $DX(\mathbf{p}_m)$ become real and positive and, hence, \mathbf{p}_m is a repelling node. Similarly, a sign analysis of the eigenvalues of $DX(\mathbf{p}_1)$ reveals the stability of \mathbf{p}_1 and the dimensions of its invariant manifolds. \square \square

Proposition 2. *If $b > g$ and $\Delta > 0$, then both equilibria \mathbf{p} and \mathbf{q} of (7) are in the domain Ω .*

Proof. It is immediate to see that if $\Delta > 0$, then \mathbf{p} and \mathbf{q} exist and are different. To see that $\mathbf{p}, \mathbf{q} \in \Omega$, note that if $b > g$ and $\Delta > 0$, then

$$\begin{aligned} bsm &> -a(b-g) \\ \Leftrightarrow 2bsm &> -4a(b-g) - 2bsm \\ \Leftrightarrow bs(m^2 + 2m + 1) &> -4a(b-g) + bs(m^2 - 2m + 1) \\ \Leftrightarrow b^2s^2(1+m)^2 &> bs\Delta \\ \Leftrightarrow bs(1+m) &> \sqrt{bs\Delta} \\ \Leftrightarrow q_u &> p_u > 0. \end{aligned}$$

Finally, since $q_v = (b-g)q_u/g$ and $p_v = (b-g)p_u/g$, the result follows. \square \square

To perform a stability analysis of the equilibria \mathbf{p} and \mathbf{q} by standard methods is a challenging task. Indeed, the Jacobian matrix of X evaluated at \mathbf{p} and \mathbf{q} are given, respectively, by

$$DX(\mathbf{p}) = \begin{pmatrix} 0 & 0 & 1 & 0 \\ 0 & 0 & 0 & 1 \\ a_{31} & a_{32} & \frac{c}{d} & 0 \\ a_{41} & a_{42} & 0 & c \end{pmatrix} \quad \text{and} \quad DX(\mathbf{q}) = \begin{pmatrix} 0 & 0 & 1 & 0 \\ 0 & 0 & 0 & 1 \\ b_{31} & b_{32} & \frac{c}{d} & 0 \\ b_{41} & b_{42} & 0 & c \end{pmatrix},$$

where

$$a_{31} = \frac{2a(bg + g^2 - 2b^2) + b(b(m-1)^2s - (m+1)\sqrt{bs\Delta})}{2bdg} p_u,$$

$$b_{31} = \frac{2a(bg + g^2 - 2b^2) + b(b(m-1)^2s + (m+1)\sqrt{bs\Delta})}{2bdg} q_u,$$

and

$$a_{32} = \frac{ag}{bd} p_u, \quad a_{41} = -(b-g)p_v, \quad a_{42} = (b-g)p_u.$$

$$b_{32} = \frac{ag}{bd} q_u, \quad b_{41} = -(b-g)q_v, \quad b_{42} = (b-g)q_u.$$

Hence, the computation of analytic expressions for the eigenvalues of $DX(\mathbf{p})$ and $DX(\mathbf{q})$ turns out to be a cumbersome goal. However, direct inspection of equilibrium coordinates reveals evidence of some local bifurcations. If $b = g$, then from (11) we have $q_v = p_v = 0$, $q_u = 1$, and $p_u = m$, since

$$\frac{bs(1+m) \pm \sqrt{b^2s^2(m-1)^2}}{2bs} = \frac{bs(1+m) \pm bs(1-m)}{2bs} = \frac{1+m \pm (1-m)}{2}.$$

This implies that $\mathbf{q} = \mathbf{p}_1$ and $\mathbf{p} = \mathbf{p}_m$. Since, according to Lemma 1, there is a stability change for \mathbf{p}_1 and \mathbf{p}_m when $b = g$, this is an indication of a transcritical bifurcation. The equilibrium points \mathbf{q} and \mathbf{p}_1 collide and interchange their stability when $b = g$; a similar statement follows for \mathbf{p} and \mathbf{p}_m . On the other hand, if $\Delta = 0$, then $q_u = p_u$ and $q_v = p_v$, so that $\mathbf{q} = \mathbf{p}$. Since these two equilibria exist only if $\Delta > 0$, this is evidence of a saddle-node (or fold) bifurcation of equilibrium points. Formal proofs for these statements require the reduction of (7) into a one-parameter family of center manifolds on each case, followed by verification of certain genericity conditions; we refer to [33, 43] for more details. However, we opt to omit these proofs in favor of a focus on the analysis of global bifurcations in (7) and the emergence of traveling waves in (5).

4. BIFURCATION ANALYSIS

In this section we present a bifurcation analysis of (7) performed with the standard continuation package AUTO. As a starting point we consider parameters $a = 24$, $b = 19$, $g = 1$ and $s = 100$ fixed throughout this section and let d and m to slowly vary. The fixed values of a, b, g and s correspond to those in [4] after the transformation (4). Moreover, we take the initial value $c = 1$ for the wave speed in (7) for a first analysis. Later in Section 9, we let c to vary in order to capture its influence on the existence and properties of the wave solutions.

The resulting bifurcation scenario in the (m, d) -plane is shown in figure 5. Of special importance for us are the curves h_p and h_q which represent homoclinic bifurcations to \mathbf{p} and \mathbf{q} , respectively. The curve h_p is divided into two segments (labeled as h_p^c and h_p^s , respectively) by a codimension two Belyakov homoclinic point, labeled as B . The right-hand side endpoints of both h_p^c and h_q (marked with \times) correspond to the last points where we could obtain convergence of the computed solutions with AUTO. We will address the details and consequences of these homoclinic bifurcations in section 5.

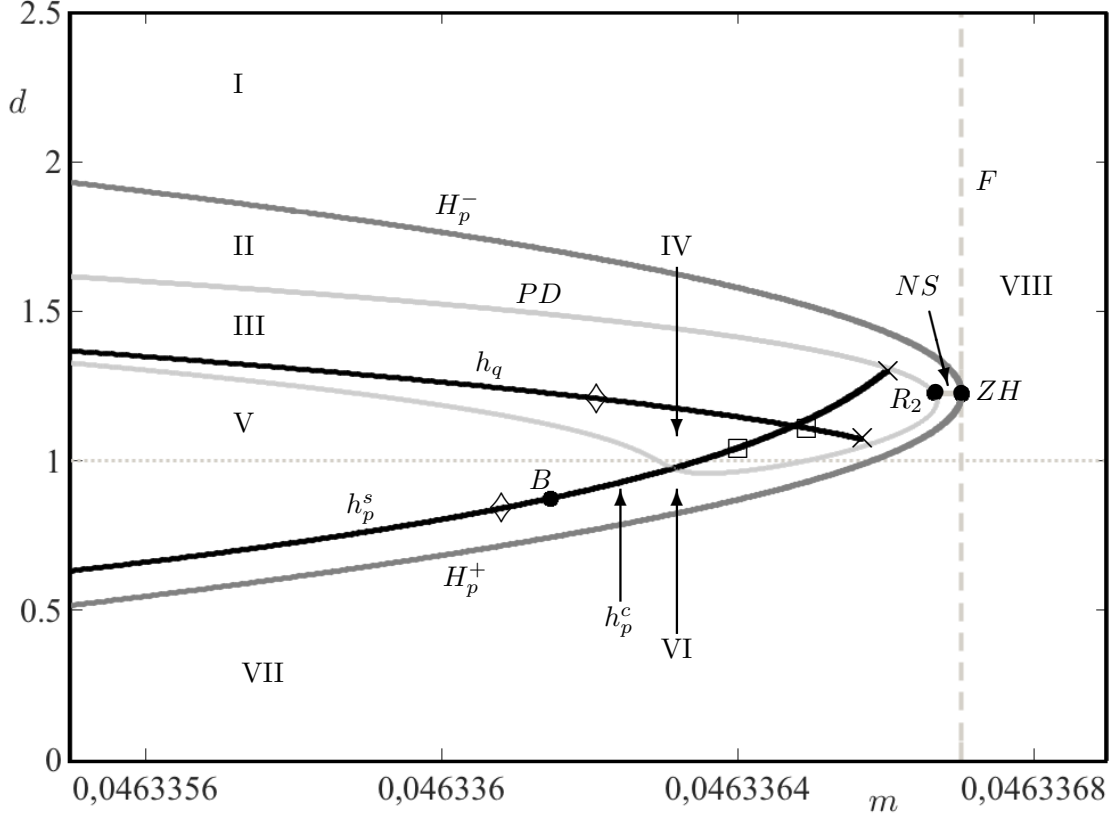


FIGURE 5. Bifurcation diagram of (7) in the (m, d) -plane space. Parameter values are the same as in figure 2.

Let us continue with an inspection of the other elements in figure 5. The first of these remaining ingredients is a curve of Hopf bifurcation at the equilibrium \mathbf{p} . This bifurcation curve is divided into two segments. The first one is a segment of supercritical Hopf bifurcation, labeled as H_p^- ; the other one is a segment of subcritical Hopf bifurcation, labeled as H_p^+ . The curve H_p^- meets a Fold bifurcation curve F in a quadratic tangency at a codimension two Zero-Hopf bifurcation point, labeled as ZH . The separation between the curves H_p^- and H_p^+ occurs at a codimension two generalized Hopf bifurcation point located very close to the ZH point; we choose not to label this generalized Hopf point in figure 5 to avoid an overlapping with the ZH point. The curve labeled as PD corresponds to a period doubling bifurcation while NS is a Neimark-Sacker (or torus) bifurcation curve. These two curves meet at a codimension two strong resonant point R_2 . The horizontal dotted line in figure 5 corresponds to $d = 1$ (or equivalently, $D_1 = D_2$ in (3)). While this line does not represent any bifurcation, it is useful to distinguish the phenomena encountered above it from that which occurs below it. Indeed, one must remember that if $d > 1$ (resp. $d < 1$), then prey have a higher (resp. lower) diffusion rate than predators.

The bifurcation curves in figure 5 divide the (m, d) -plane into the open regions I-VIII. Region VIII is bounded to the left by the curve F , while I is delimited to its right by F , and below by H_p^- . Region II is surrounded by the curves H_p^- , NS , and PD ; while region III is enclosed by the curves PD , h_p^+ , and h_q . Furthermore, region IV is bounded by the segments h_q , h_p^+ , and PD , while region V is surrounded by the curves PD , h_p^- , and h_p^+ . Finally, region VI is enclosed by the curves h_p^- , h_p^+ , PD , NS , and H_p^+ , while region VII is delimited to the right by the curve F and above by H_p^+ .

It is relevant to note that the fold curve F corresponds to $\Delta = 0$ in section 3. Hence, equilibrium points \mathbf{p} and \mathbf{q} exist on the left-hand side of the F curve (regions I-VII). In particular, if $(m, d) \in \text{I}$, both equilibria are hyperbolic. If (m, d) passes through the supercritical Hopf bifurcation curve H_p^- from region I towards region II, a limit cycle branches out from \mathbf{p} . While the Hopf bifurcation is supercritical, this criticality is restricted only to a suitable two-dimensional center manifold where the bifurcation takes place [33, 43]; the resulting periodic orbit in \mathbb{R}^4 is, in fact, of saddle type in region II. The stability properties of this cycle remain unchanged until this orbit undergoes a period doubling bifurcation when $(m, d) \in PD$. This periodic orbit faces a number of further bifurcations (not shown in figure 5) as the point (m, d) moves towards the curve h_q where it gives rise to a homoclinic orbit. We will address this transitions again in section 6. On the other hand, if the point (m, d) crosses the NS curve from region II into region VI, an invariant torus bifurcates as a periodic orbit undergoes a Neimark-Sacker bifurcation.

Our bifurcation diagram in figure 5 is just partially complete. Other codimension two strong resonances can be found along the NS bifurcation curve. Although the complete bifurcation diagram near these bifurcation points is yet to be known in its full complexity, one should expect the appearance of chaotic behavior when the point (m, d) is in a neighborhood of the NS curve; for further details, see [43]. Furthermore, bifurcation theory tells us that there is an infinite number of bifurcation curves in neighborhoods of both points B and R_2 . However, the full bifurcation picture near each of these points is not fully known from a theoretical point of view [43]. (We will address the complex dynamics that emerges due to the point B in section 5 below).

5. HOMOCLINIC BIFURCATIONS, WAVE PULSES, AND CHAOS

Figure 6 shows three different homoclinic orbits to the equilibrium \mathbf{p} in the left-hand side column, and their respective time series in the right-hand side column. The values of parameters (m, d) for each case correspond to those marked as \diamond , \square and \times along the curve h_p in figure 5. In the left-hand side column of figure 6, the homoclinic trajectories develop a rotational movement near \mathbf{p} before making a large excursion and returning to \mathbf{p} ; see the sequence of panels (a1)-(b1)-(c1). The amplitude of these oscillations increases as the point (m, d) moves to the right along the curve h_p . As a result, the corresponding wave pulses in panels (a2)-(b2)-(c2) feature an initial transient with increasingly larger oscillations —as (m, d) moves to the right along h_p — around the equilibrium values; in each case, this culminates in a large pulse before decaying back to the rest state. Indeed, the initial pattern of smaller amplitude oscillations of each wave takes most of a long interval of values of $z \in]0, 1[$ (i.e, it is a “slow” build-up in terms of z); while the large amplitude pulse occurs in a smaller interval (of order 10^{-4}) of parameter z (i.e, a “fast” discharge). Further, notice that both populations tend to increase and decrease their densities simultaneously along any given traveling pulse.

The existence of the homoclinic orbit to \mathbf{p} implies the presence of chaotic dynamics. Let us now state the main reasons for this claim. For any (m, d) in a neighbourhood of the curve h_p , the linearization of (7) at the equilibrium \mathbf{p} has one (stable) eigenvalue $\lambda^s < 0$ and three (unstable) eigenvalues $\lambda_{1,2}^u \in \mathbb{C}$, and $\lambda_3^u > 0$. In particular, $\lambda_{1,2}^u$ are complex conjugate with positive real part $\text{Re}(\lambda_{1,2}^u) > 0$. The equilibrium \mathbf{p} is called a *saddle-focus*. Figure 7 shows all the possible values of the eigenvalues of \mathbf{p} (in the complex plane) along the computed segment of the homoclinic bifurcation curve h_p . Namely, as parameters (m, d) are allowed to vary along the computed segment of the curve h_p in figure 5, each

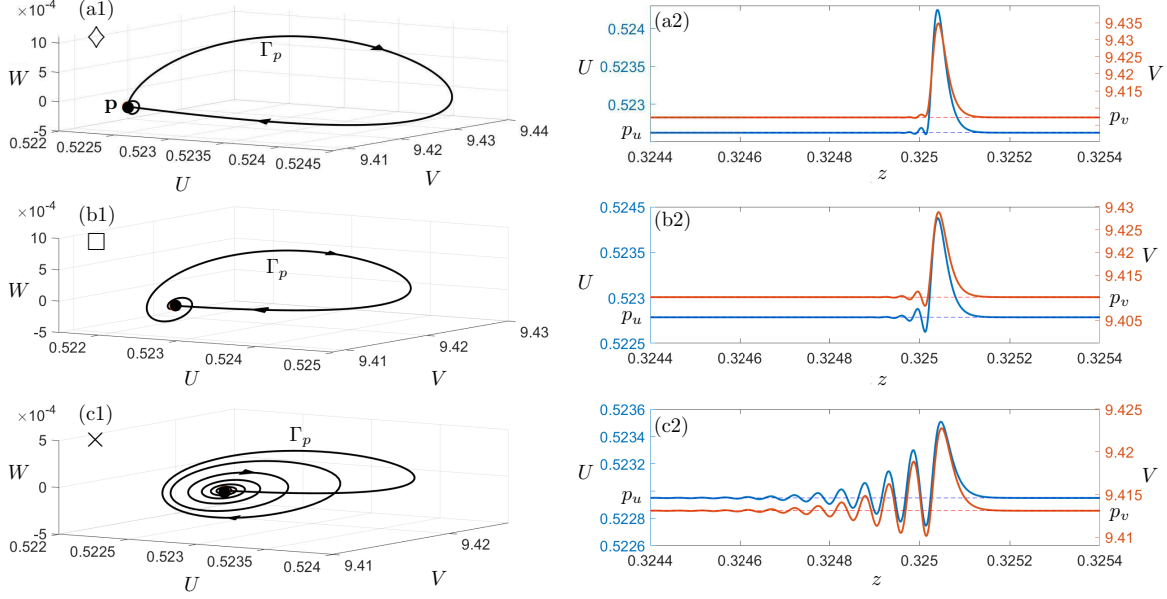


FIGURE 6. Homoclinic orbits to the equilibrium \mathbf{p} along the bifurcation curve h_p . Parameter values are $(m, d) = (0.0463361, 0.8740509)$ in panels (a1)-(a2), $(m, d) = (0.0463364, 1.0390163)$ in panels (b1)-(b2), and $(m, d) = (0.0463366, 1.2995479)$ in panels (c1)-(c2). The other parameters values are the same as in figure 2.

eigenvalue of \mathbf{p} traces out a curve segment whose plots are shown in figure 7. Among the unstable eigenvalues, the pair $\lambda_{1,2}^u$ are the closest to the imaginary axis $\text{Re}(\lambda) = 0$; hence, we say that $\lambda_{1,2}^u$ are the *leading unstable* eigenvalues. In this setting, if we define the so-called *saddle quantity* as $\sigma_1 = \lambda^s + \text{Re}(\lambda_{1,2}^u)$, Shilnikov's theorems [33, 43] state that if $\sigma_1 > 0$, the homoclinic bifurcation is *simple* or *mild*. In this simple Shilnikov homoclinic bifurcation, a single (repelling) periodic orbit bifurcates from the homoclinic orbit on one side of the curve h_p . On the other hand, if $\sigma_1 < 0$, the homoclinic bifurcation is chaotic and gives rise to a wide range of complicated behaviour in phase space. More specifically, one can find horseshoe dynamics in return maps defined in a neighbourhood of the homoclinic orbit. The suspension of the Smale horseshoes forms a hyperbolic invariant chaotic set which contains countably many periodic orbits of saddle-type. The horseshoe dynamics is robust under small parameter perturbations, i.e., the chaotic dynamics persist if the homoclinic connection is broken; see [33, 43]. The segments labeled as h_p^s and h_p^c in figure 5 correspond to simple and chaotic regimes, respectively, and are separated by the Belyakov point B where $\sigma_1 = 0$ [13]. (Actually, at $(m, d) = B$, we have $\text{Re}(\lambda_{1,2}^u) = |\lambda^s| \approx 0.6654466$). Likewise, in figure 7, the segments h_p^s and h_p^c along the curves for $\lambda_{1,2}^u$ correspond to $\sigma_1 > 0$ (simple) and $\sigma_1 < 0$ (chaotic), respectively, and are separated by the point labeled as B where $\sigma_1 = 0$. This same Belyakov transition is shown for the corresponding λ^s value as well (and is also labeled as B).

The bifurcation picture near the curve h_p in figure 5 is just a partial representation of the full complexity one may encounter in this region of parameter space. Indeed, the saddle periodic orbits associated with the invariant chaotic set may also undergo further bifurcations such as period-doubling and torus bifurcations [33, 43]. Moreover, the presence of the chaotic h_p^c bifurcation and that of the Belyakov point B imply a very complicated structure (not shown) of infinitely many saddle-node and period-doubling bifurcations of periodic orbits as well as of subsidiary n -homoclinic orbits. Figure 8

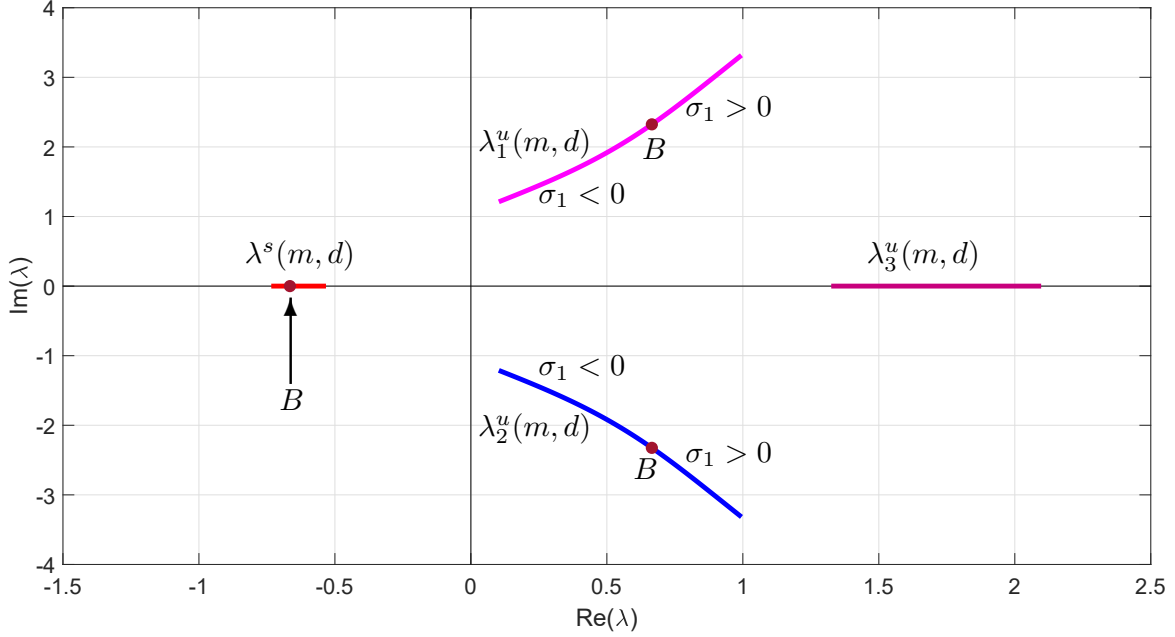


FIGURE 7. Eigenvalues of the Jacobian matrix $DX(\mathbf{p})$ continued for every (m, d) along the homoclinic bifurcation curve h_p in figure 5.

shows a 2-homoclinic orbit to \mathbf{p} (in panel (a1)) and a 4-homoclinic orbit to \mathbf{p} (in panel (b1)), as well as their corresponding time series in panels (a2) and (b2), respectively. In general, n -homoclinic orbits are characterized by making $n - 1$ close passes near the equilibrium before closing up to form the connection; see panels (a1) and (b1). As a consequence, the corresponding traveling wave develops n pulses before setting down to the steady state values; see the 2-pulse and 4-pulse waves in panels (a1) and (b1), respectively. Moreover, for each of these subsidiary n -homoclinic orbits, the system exhibits horseshoe dynamics and chaos as in the original homoclinic scenario.

As for the homoclinic bifurcation h_q at the equilibrium \mathbf{q} , the associated Jacobian matrix of (7) at \mathbf{q} has a pair of complex-conjugate stable eigenvalues $\mu_{1,2}^s \in \mathbb{C}$ and a pair of complex-conjugate unstable eigenvalues $\mu_{1,2}^u \in \mathbb{C}$, with $\text{Re}(\mu_{1,2}^s) < 0$ and $\text{Re}(\mu_{1,2}^u) > 0$. The structure of the eigenvalues of \mathbf{q} as a function of $(m, d) \in h_q$ is shown in figure 9. We say that \mathbf{q} is a *focus-focus* or *bi-focus*. The resulting homoclinic orbit Γ_q features a spiral-type convergence to \mathbf{q} as $z \rightarrow \pm\infty$. Figure 10 shows three different examples of such homoclinic orbit in the left column, and their respective time series in the right one. The values of parameters (m, d) for each case correspond to those marked as \diamond , \square and \times along the curve h_q in figure 5. In the left-hand side column of figure 10, the amplitude of the oscillations increases as the point (m, d) moves to the right along the curve h_q . As a result, the corresponding wave pulses in panels (a2)-(b2)-(c2) develop more oscillations —as (m, d) moves to the right along h_q — before converging to the equilibrium values as $z \rightarrow \infty$. The spirals and oscillations that are visible in panels (a1)-(b1)-(c1) and in panels (a2)-(b2)-(c2), respectively, are associated with the stable eigenvalues $\mu_{1,2}^s$ of \mathbf{q} . There is another set of oscillations as $z \rightarrow -\infty$ which are associated with the unstable eigenvalues $\mu_{1,2}^u$; however, since $\text{Im}(\mu_{1,2}^u) < \text{Im}(\mu_{1,2}^s)$ (see figure 9 again), these spirals are relatively less pronounced and hard to see in figure 10. Nevertheless, like the case of the homoclinic orbit to \mathbf{p} , here both populations tend to increase and decrease their densities simultaneously along any given traveling pulse.

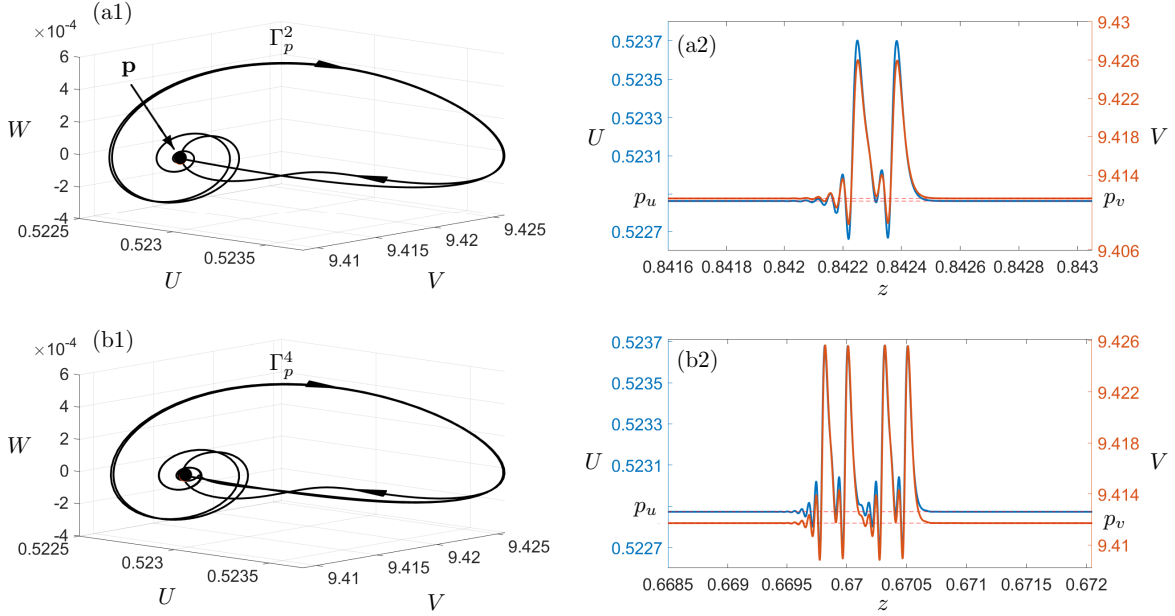


FIGURE 8. Panel (a1) shows Γ_p^2 , the 2-homoclinic orbit to \mathbf{p} , while panel (a2) shows its time series of U and V associated with Γ_p^2 . Similarly, panels (b1)-(b2) show a 2-homoclinic orbit and its associated 4-pulse wave, respectively. Parameter values are the same as in figure 2 except for $(m, d) = (0.0463361, 1.1533894)$ in panels (a1)-(a2) and $(m, d) = (0.0463365, 1.1683875)$ in panels (b1)-(b2).

The homoclinic bifurcation at the focus-focus equilibrium \mathbf{q} induces chaotic dynamics for every $(m, d) \in h_q$. Indeed, the presence of the homoclinic orbit Γ_q to a focus-focus equilibrium is accompanied by horseshoe dynamics in cross sections near Γ_q and, hence, an infinite number of saddle periodic orbits in a neighbourhood of Γ_q [43, 55]. Furthermore, in this setting, the *saddle quantity* is defined as $\sigma_2 = \text{Re}(\mu_{1,2}^s) + \text{Re}(\mu_{1,2}^u)$. Since $\sigma_2 > 0$ for every $(m, d) \in h_q$, it follows that there are no stable periodic orbits near Γ_q [27, 38].

In sum, any solution in a neighborhood of either Γ_p (in the chaotic case) or Γ_q tends to behave erratically and presents sensitive dependence to initial conditions. The corresponding orbit in the four-dimensional phase space of (7) spends a long transient visiting a strange hyperbolic invariant set before converging to an attractor. Hence, any bounded solution of (7) passing near either Γ_p (in the h_p^c side of the bifurcation) or Γ_q is associated with a chaotic traveling wave, making spatial population dynamics to behave in an unpredictable way [55].

Figure 11(a) shows both homoclinic orbits Γ_p and Γ_q coexisting in phase space, while figures 11(b1) and 11(b2) show the time series of U and V associated with either trajectory. This special configuration occurs when the bifurcation curves h_p^c and h_q cross each other at $(m, d) \approx (0.046336476, 1.11668)$; see the bifurcation diagram of figure 5). While this intersection point is not a new bifurcation, at these parameter values both classes of homoclinic orbits, Γ_q and Γ_p , coexist in phase space. Moreover, one obtains the coexistence of both chaotic invariant sets (each associated with one of the homoclinic trajectories) and, hence, the corresponding erratic behaviour and sensitive dependence on initial conditions of nearby solutions.

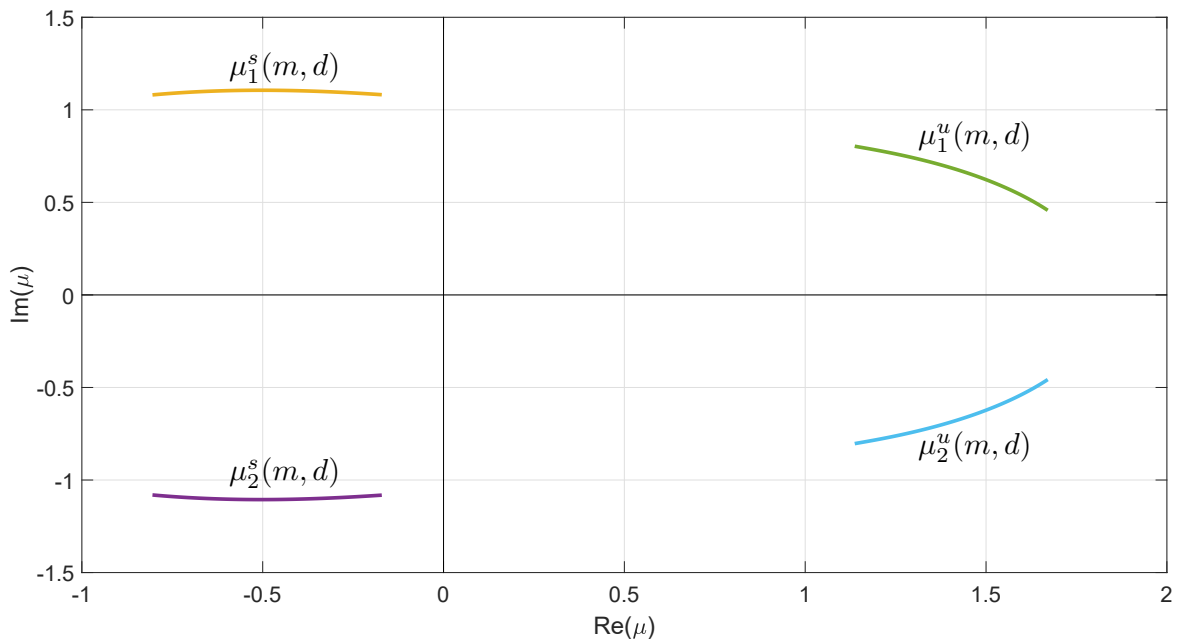


FIGURE 9. Eigenvalues $\mu_1^s(m, d)$, $\mu_2^s(m, d)$, $\mu_3^u(m, d)$ and $\mu_4^u(m, d)$ of $DX(\mathbf{q})$ continued for every (m, d) along the homoclinic bifurcation curve h_q in figure 5.

6. PERIODIC ORBITS AND WAVE TRAINS

In this section we study the limit cycles existing in (7), their bifurcations, and their consequences for the nature of wave trains.

6.1. Period doubling phenomena. Let us consider the periodic orbit Γ which originates at the supercritical Hopf bifurcation H_p^- and track its successive bifurcations as parameter d is decreased and $m = 0.0463358$ remains fixed. When (m, d) crosses the PD curve from region II to III, the cycle Γ undergoes a period doubling bifurcation. As (m, d) enters region III, Γ changes its stability and a secondary limit cycle Γ^2 appears with approximately twice the period of Γ . As parameter d is further decreased, additional period doubling events occur (not shown in figure 5). This is illustrated in figure 12. Periodic orbits Γ^2 , Γ^4 and Γ^8 of periods 2, 4, and 8 times that of Γ , respectively, are shown in panels (a1)-(b1)-(c1). Panels (a2)-(b2)-(c2) show one period of the corresponding time series of U and V . Here the actual periods of the solutions are rescaled to $T = 1$ for visualization and computational purposes (We explain more about the numerical method to obtain these periodic orbits in the Appendix A). As a consequence, as parameter d decreases and system (7) undergoes this sequence of period doubling bifurcations, the associated wave trains in panels (a2)-(b2)-(c2) display periodic spatio-temporal patterns with doubling periods.

6.2. Transition from wave trains to wave pulses. It is essential to highlight that when the point (m, d) crosses the PD curve from region II to region III, the cycle Γ does not disappear but just changes its stability. Figure 13 shows the graph of the period T of this cycle as a function of d . The bifurcation curve oscillates around the critical value $d^* = 1.3080156$ for which the homoclinic bifurcation h_q to \mathbf{q} occurs. The amplitude of the oscillations decreases rapidly as the homoclinic limit is approached when d tends to d^* ; see [43] and the references therein. Indeed, the “snaking” behavior of the bifurcation curve

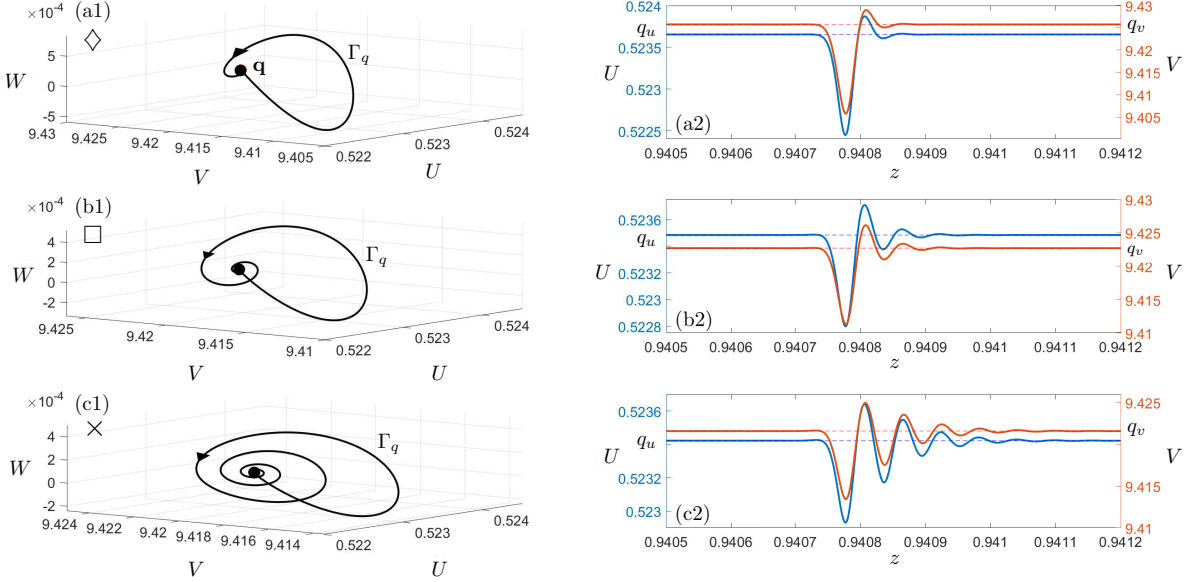


FIGURE 10. Homoclinic orbits to the equilibrium \mathbf{q} along the bifurcation curve h_q . Parameter values are $(m, d) = (0.0463362, 1.2091095)$ in panels (a1)-(a2), $(m, d) = (0.0463365, 1.1092036)$ in panels (b1)-(b2), and $(m, d) = (0.0463366, 1.0724625)$ in panels (c1)-(c2). The other parameters values are the same as in figure 2.

is typical of the main branch of periodic orbits near chaotic saddle-focus and focus-focus homoclinic bifurcations [27, 63]. At each of the infinitely many folds of the curve a pair of periodic orbits is created via a saddle-node bifurcation of limit cycles. Some of the periodic orbits in this branch may further undergo period-doubling bifurcations changing their stability along the bifurcation curve. Figure 14 shows three such periodic orbits, labelled as Γ_A , Γ_B , and Γ_C , respectively, corresponding to the points A , B and C in figure 13. As d approaches d^* , the cycles pass increasingly closer to \mathbf{q} (see the sequence of panels (a1)-(b1)-(c1) in figure 14). As a result, one obtains wave trains which spend longer transients close to the equilibrium values (see the sequence of panels (a2)-(b2)-(c2) in which the period T of each cycle is rescaled to 1). Hence, one can think of the homoclinic orbit Γ_q (and its corresponding wave pulse) as the limit of this sequence of periodic orbits (resp. wave trains) of increasing period as $d \rightarrow d^*$. Furthermore, each of the periodic orbits bifurcated from the period doubling phenomena in subsection 6.1 may also increase their periods and undergo a convergence to n -homoclinic orbits in a similar fashion. Some of these secondary homoclinic bifurcations are mentioned before in section 5 and shown in figure 8.

7. HETEROCLINIC CONNECTIONS AND WAVE FRONTS

Figure 15(a) shows a heteroclinic orbit, labeled as $\Gamma_{q,p}$, obtained for $(m, d) = (0.0463358, 2.4)$ in region I. The heteroclinic connection is oriented from \mathbf{q} to \mathbf{p} as parameter z —that which parameterizes the curve—is increased. The resulting time series are shown in figure 15(b) and they correspond to a wave front traveling from the steady state \mathbf{q} that decays exponentially to \mathbf{p} in synchronized oscillatory fashion. This non-monotonic behavior is explained by the presence of a pair of stable

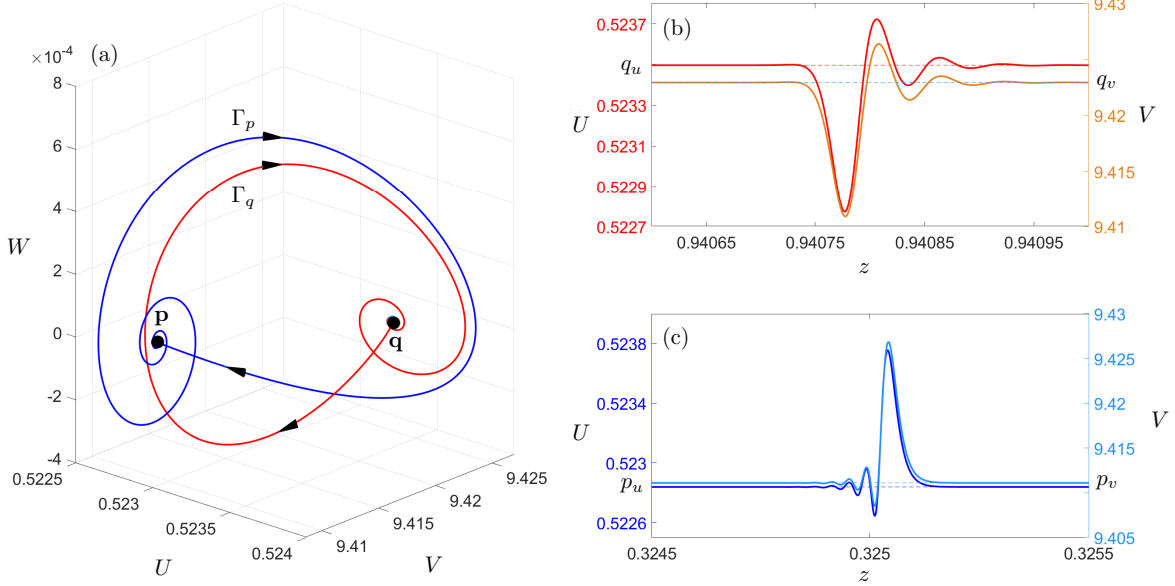


FIGURE 11. Panel (a) shows a projection of Γ_s and Γ_p onto the UVW space, when $(m, d) \approx (0.046336476, 1.11668) \in h_p^c \cap h_q$. Meanwhile, panel (b1) (resp. (b2)) shows the time series of U and V rendered in different color tones, associated with Γ_s (resp. Γ_p). The other parameter values are the same as in figure 2.

complex-conjugate eigenvalues (with negative real part) of \mathbf{p} when parameters (m, d) are in region I. The connecting orbit $\Gamma_{q,p} \subset W^s(\mathbf{p}) \cap W^u(\mathbf{q})$ lies in the intersection of the global invariant manifolds $W^s(\mathbf{p})$ and $W^u(\mathbf{q})$. Namely, $\Gamma_{q,p}$ is contained in the two-dimensional unstable manifold $W^u(\mathbf{q})$ — computed with the method in the Appendix A, and represented in figure 15(a) as a transparent red surface — and approaches \mathbf{p} along its three-dimensional stable manifold $W^s(\mathbf{p})$. Moreover, since $W^s(\mathbf{p})$ and $W^u(\mathbf{q})$ are, respectively, three and two-dimensional immersed smooth manifolds in \mathbb{R}^4 , it follows that the intersection $W^s(\mathbf{p}) \cap W^u(\mathbf{q})$ is transverse [35]. As a consequence, the heteroclinic orbit $\Gamma_{q,p}$ and, hence, its associated wave front persist under small parameter variations. Under small changes to the parameter values in region I, the resulting wave front may vary the amplitude of its oscillations and the actual asymptotic values, but the qualitative behavior of the traveling front remains unaltered throughout.

As parameter (m, d) crosses the H_p^- curve from region I to region II, a pair of stable eigenvalues of \mathbf{p} cross the imaginary axis and become unstable; in the process, a limit cycle branches from \mathbf{p} in a supercritical Hopf bifurcation. Hence, in region II, $W^s(\mathbf{p})$ is a one-dimensional manifold and the connection $\Gamma_{q,p}$ does not exist. Rather, it is replaced by a heteroclinic orbit that joins \mathbf{q} to the bifurcated cycle. Figure 16(a) shows the bifurcated periodic orbit, labeled as γ after (m, d) has entered region II from region I. The unstable manifold $W^u(\mathbf{q})$ rolls up around γ and intersects the three-dimensional stable manifold $W^s(\gamma)$ transversally along a heteroclinic orbit, labeled as $\Gamma_{q,\gamma}$. This heteroclinic connection is associated with the traveling wave shown in figure 16(b); this is a front transitioning from the steady state at \mathbf{q} into a periodic pattern around \mathbf{p} . The heteroclinic orbit $\Gamma_{q,\gamma}$ (and its traveling front) is preserved in an open subset of region II, and it disappears when (m, d) crosses the PD curve towards region III as γ loses its stability in a period doubling bifurcation.

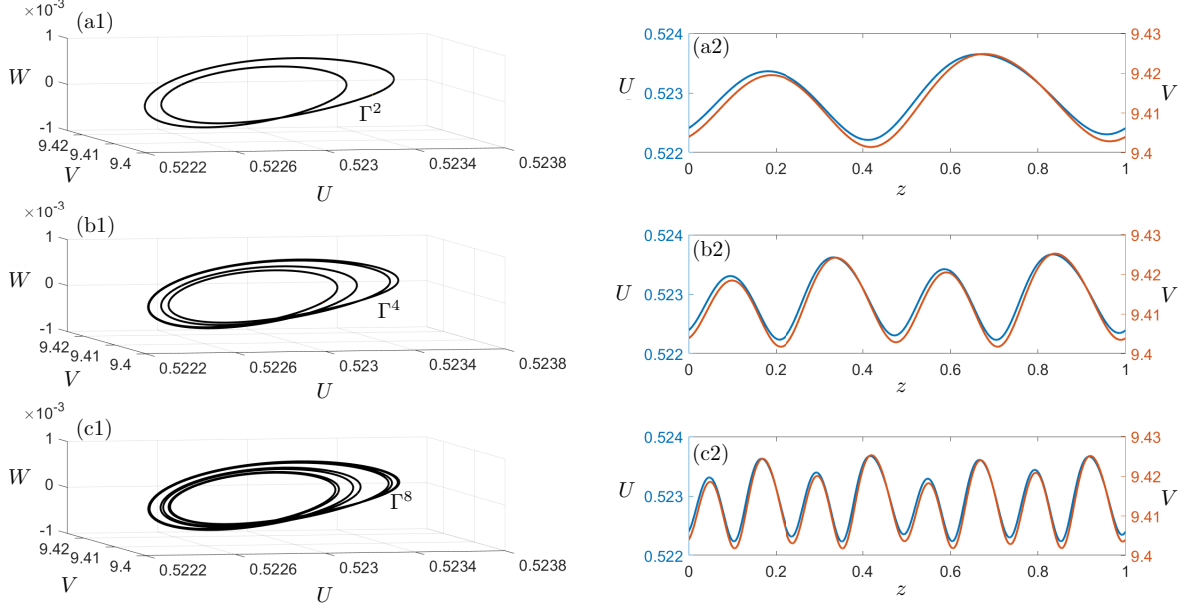


FIGURE 12. The different periodic orbits (panels (a1), (b1) and (c1)) and associated wave trains (panels (a2), (b2) and (c2)) emerging from successive period doubling bifurcations. While the periods in the time series are uniformly rescaled to 1 for computational purposes, the actual periods of the cycles are $T = 12.1829$ for Γ^2 , $T = 24.3659$ for Γ^4 , and $T = 48.7318$ for Γ^8 . Parameter values are $d = 1.469369$ (in panels (a)), $d = 1.4607309$ (in panels (b)), and $d = 1.4590971$ (in panels (c)), with $m = 0.0463362$ fixed. The other parameters are as in figure 2.

If (m, d) is in an open subset of regions III, IV, and V, one can find a wave front traveling from \mathbf{p} to \mathbf{q} . This front travels in the opposite direction to that in figure 15 and, hence, it corresponds to a third kind of wave. The wave front traveling from \mathbf{p} to \mathbf{q} is shown in figure 17(b). The wave begins at the steady state \mathbf{p} with oscillations of increasing amplitude until it settles at \mathbf{q} . This front corresponds to an intersection of the manifolds $W^s(\mathbf{q})$ and $W^u(\mathbf{p})$ forming a heteroclinic orbit in the phase space of (7); figure 17(a) shows the heteroclinic orbit (labelled as $\Gamma_{p,q}$) and the two-dimensional manifold $W^s(\mathbf{q})$ of \mathbf{q} as a transparent blue surface. The connection $\Gamma_{p,q}$ is an orbit in the three dimensional unstable manifold $W^u(\mathbf{p})$ which lies on $W^s(\mathbf{q})$ to converge to \mathbf{q} .

8. MULTIPLE WAVE FRONTS AT THE FOCUS-FOCUS HOMOCLINIC BIFURCATION

In section 5 we described the complicated dynamics that can be found near the focus-focus homoclinic bifurcation Γ_q when $(m, d) \in h_q$. One of the consequences of this fact is the appearance of multiple wave fronts of type $\Gamma_{p,q}$ (described in section 7) which coexist with the main wave pulse Γ_q . We explain this finding here by direct, close inspection of the invariant manifolds involved.

Figure 18 shows the projection of $W^s(\mathbf{q})$ onto the UVW space, when $(m, d) \approx (0.0463358, 1.3080156) \in h_q$. Also shown is the homoclinic orbit Γ_q (red curve). The two-dimensional manifold $W^s(\mathbf{q})$ is rendered as a transparent blue surface. Some orbits in $W^s(\mathbf{q})$ lie in the three-dimensional unstable manifold $W^u(\mathbf{p})$ forming heteroclinic connections. In our computations, we detected seven heteroclinic orbits contained in $W^u(\mathbf{p}) \cap W^s(\mathbf{q})$; the method to detect them is explained in the Appendix A. Most of

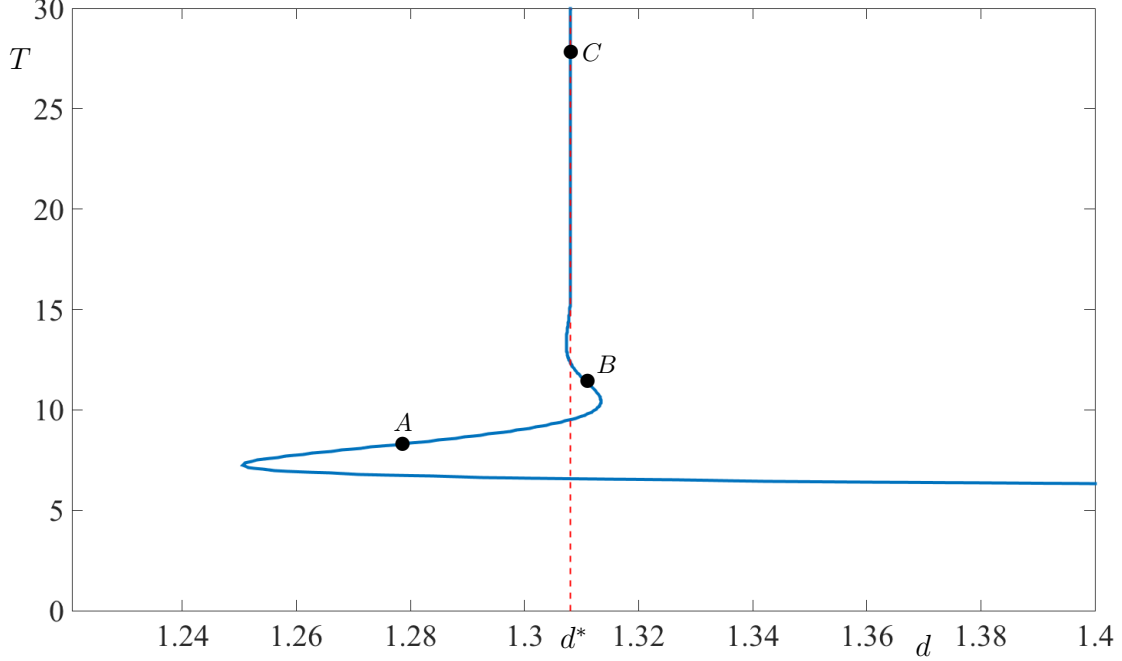


FIGURE 13. Bifurcation curve of the period T of periodic orbits with respect to d , near the homoclinic bifurcation at \mathbf{p} . Here $m = 0.0463358$ is fixed and the other parameters as are as in figure 2.

these heteroclinic connections are very close to one another and very hard to distinguish from each other; we show one of them (cyan curve labeled as $\Gamma_{p,q}$) in figure 18. Each of these seven heteroclinic orbits correspond to a different wave front traveling from \mathbf{p} to \mathbf{q} which are present in the system at the same time. Further, there are also 2- and 3-homoclinic orbits to \mathbf{q} in $W^u(\mathbf{q}) \cap W^s(\mathbf{q})$ coexisting with the primary homoclinic orbit and the heteroclinic connections in phase space; we opted to not show these subsidiary homoclinic orbits in figure 18 for visualization purposes. Figure 19(a) shows the spatial profiles of the prey U associated with the primary wave pulse Γ_q and the secondary 2- and 3-pulse waves (labeled as Γ_q^2 and Γ_q^3 , respectively) associated with the secondary homoclinic orbits. In turn, figure 19(b) shows three representative traveling fronts associated with the family of heteroclinic orbits in phase space. The existence of these families of wave fronts when $(m, d) \in h_q$ indicates that there must be a sequence of associated global bifurcations as (m, d) approaches the h_q curve. At each of these bifurcation events, the manifolds $W^u(\mathbf{p})$ and $W^s(\mathbf{q})$ intersect tangentially in \mathbb{R}^4 along a (newly created) heteroclinic orbit. As (m, d) moves closer to the h_q curve, the intersection becomes transversal and the heteroclinic orbit persists under small parameter variations. Similar events happen in the case of the secondary homoclinic orbits with $W^u(\mathbf{q})$ and $W^s(\mathbf{q})$ that explain the emergence of 2- and 3-pulse waves as parameters (m, d) approach the h_q curve.

9. THE INFLUENCE OF PROPAGATION SPEED AND DIFFUSION RATIO

The study and results reported so far in sections 4–8 were produced with fixed wave speed $c = 1$. Here we ask ourselves if there is a minimum wave speed needed for the existence of some of the traveling waves we have found. To this end, we consider the homoclinic orbits Γ_p and Γ_q existing at the curves h_p

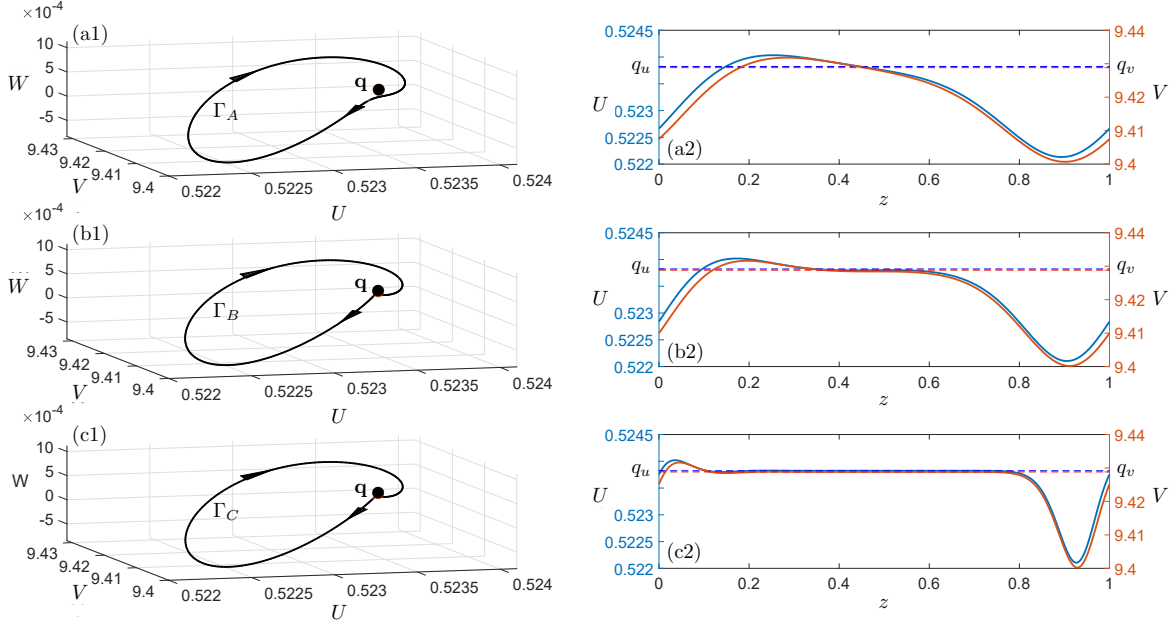


FIGURE 14. The different periodic orbits Γ_A , Γ_B and Γ_C (in panels (a1), (b1) and (c1)) and associated wave trains (panels (a2), (b2) and (c2)). While the periods in the time series are uniformly rescaled to 1 for computational purposes, the actual periods of the cycles are $T = 8.2967$ for Γ_A , $T = 11.4382$ for Γ_B , and $T = 27.8801$ for Γ_C . Parameter values are $d = 1.2785$ (in panels (a)), $d = 1.3107$ (in panels (b)), and $d = 1.3080$ (in panels (c)), with $m = 0.0463358$ fixed. The other parameters as are as in figure 2.

and h_q , respectively, when $m \approx 0.0463358$, and continue them in parameters c and d . Figure 20 shows the homoclinic bifurcation curves h_p and h_q in the (c, d) -plane. The existence of both homoclinic orbits is determined by a positive correlation between the wave speed c and the diffusion ratio d ; namely, as c decreases the wave pulses exist provided d becomes sufficiently small, or equivalently, as the predator diffusion coefficient grows larger compared to the prey diffusion coefficient.

In the case of h_p , the relation between c and d in figure 20 is almost linear for $c \geq 0.1$. Indeed the curve h_p can be approximated as $d \approx 0.2925828c + 0.4333269$, for $0.1 \leq c < 1$, with a root mean square error $e = 0.00521$. In particular, the computed segment of the curve h_p is located in the halfspace $d < 1$. Hence this kind of pulse wave with small wave speed $c < 1$ occurs only if the predator population propagates in a more efficient way than the prey. On the other hand, as c decreases below 0.01, the diffusion ratio d drops abruptly in a non linear way in the form $d = \mathcal{O}(c^{1/2})$; see figure 20(c). As c is further decreased, the continuation procedure loses precision and the last point where we get convergence of the numerical scheme is at $c_{\min} = 0.0016767$. Figure 21 shows the homoclinic orbit Γ_p when $(c, d) = (0.0479321, 0.4449391)$ in panel (a) and its corresponding time series in panel (b). In panel (a), the orbit Γ_p performs many low-amplitude turns in $W_{\text{loc}}^u(\mathbf{p})$ before developing the long excursion. The corresponding wave in panel (b) shows a slow pattern (in terms of z) of small amplitude oscillations followed by a fast large amplitude pulse in a small interval (of order 10^{-4}) of parameter z , similar to typical dynamic behaviours with different time scales. Indeed, if the relation $d = \mathcal{O}(c^{1/2})$ still holds for $c \rightarrow 0$, then both (6) and (7) become singular as $c \rightarrow 0$ and $d \rightarrow 0$; while these systems in the singular limit may be studied with tools from geometric singular perturbation theory [26], this

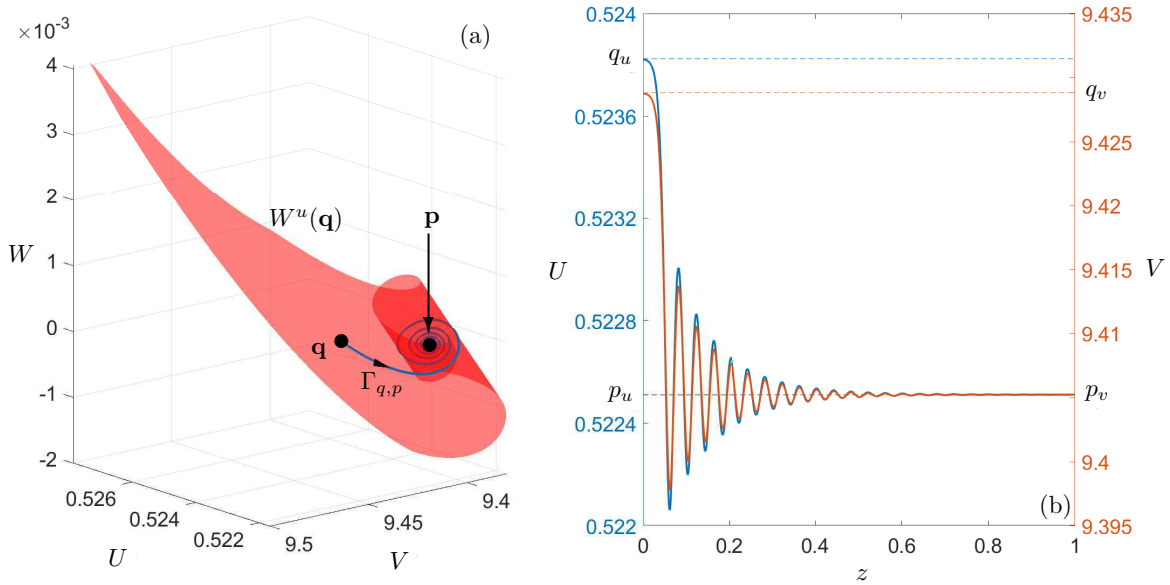


FIGURE 15. The connecting orbit $\Gamma_{q,p} \subset W^s(\mathbf{p}) \cap W^u(\mathbf{q})$ lies in the intersection of the global invariant manifolds $W^s(\mathbf{p})$ and $W^u(\mathbf{q})$ in panel (a). In panel (b) the associated wave front travels from the steady state \mathbf{q} and its amplitude decays exponentially fast to \mathbf{p} showing oscillations. Parameter values are $(m, d) = (0.0463358, 2.4)$ and the other parameters remain fixed as in figure 2.

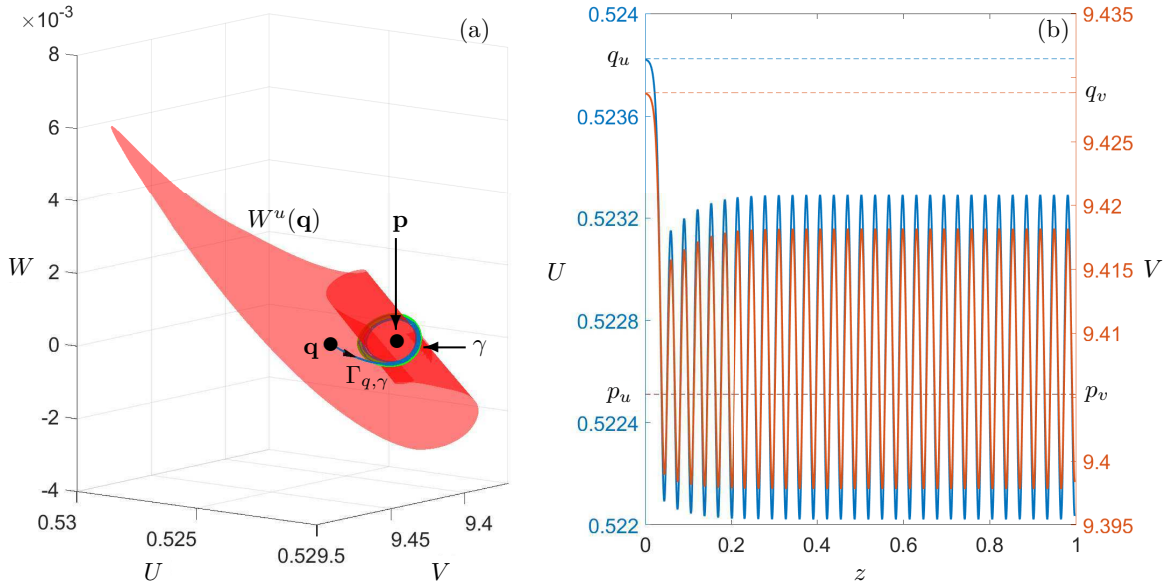


FIGURE 16. The connecting orbit $\Gamma_{q,\gamma} \subset W^s(\gamma) \cap W^u(\mathbf{q})$ lies in the intersection of the global invariant manifolds $W^s(\gamma)$ and $W^u(\mathbf{q})$ in panel (a). The associated wave front travels from the steady state \mathbf{q} and adopts a periodic behaviour oscillating around the equilibrium values of \mathbf{p} in panel (b). Parameter values are $(m, d) = (0.0463358, 1.7)$ and the other parameters remain fixed as in figure 2.

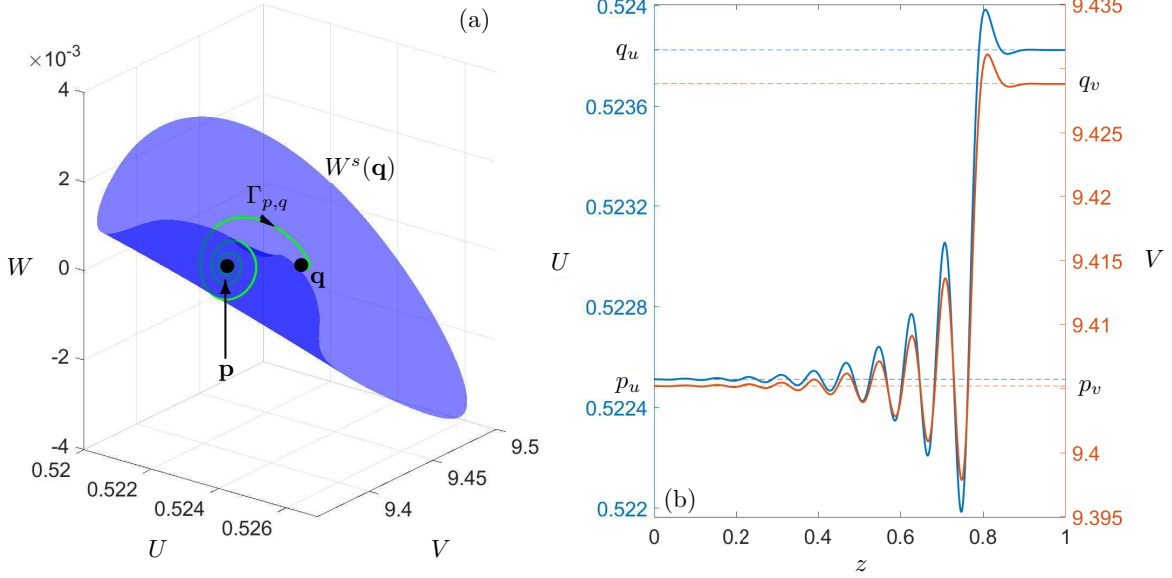


FIGURE 17. The connecting orbit $\Gamma_{p,q} \subset W^u(\mathbf{p}) \cap W^s(\mathbf{q})$ lies in the intersection of the global invariant manifolds $W^u(\mathbf{p})$ and $W^s(\mathbf{q})$ in panel (a). In panel (b) the associated wave front travels from the steady state \mathbf{p} and its amplitude increases exponentially fast before settling down at \mathbf{q} . Parameter values are $(m, d) = (0.0463358, 1.4)$ and the other parameters remain fixed as in figure 2.

is beyond the scope of this work. Nevertheless, solutions $u(x, t) = U(x + ct)$, $v(x, t) = V(x + ct)$ of (5) as $c \rightarrow 0$ and $d = D_1/D_2 \rightarrow 0$ correspond to stationary waves in which, effectively, only the predator propagation is observable in the length scale x .

As for the bifurcation curve h_q in figure 20(a)-(b), the dependence between c and d is approximately quadratic. The homoclinic orbit to the focus-focus \mathbf{q} exists whenever c and d satisfy $d \approx 0.0437881c^2 - 0.0016566c + 1.2656854$, for $0 \leq c \leq 1$; the root mean square error of this approximation is $e = 6.8 \times 10^{-5}$. In particular, the computed segment of the curve h_q is located in the half-space $d > 1$. Hence, this kind of pulse wave with small wave speed $c < 1$ occurs only if the prey population propagates in a more efficient way than the predators. Moreover, the numerical evidence suggests that the pulse wave exists for every $c > 0$ arbitrarily small, i.e., there is no positive minimum value for the wave speed c . Indeed, the bifurcation curve h_q can be continued down to $c_{\min} = 0$ with $d_{\min} \approx 1.2656854$. (In particular, the value $d_{\min} > 0$ prevents (6) and (7) to become singular, unlike the case of h_p). In the limit as $c \rightarrow 0$, the resulting wave pulse corresponds to a stationary solution of (5) where both species propagate with diffusion ratio $D_1/D_2 = d_{\min}$.

10. TRAVELING WAVES IN THE ABSENCE OF THE PREDATOR

System (7) has two invariant planes given by

$$\Pi_U = \{(U, V, W, R) \in \mathbb{R}^4 : V = R = 0\},$$

and

$$\Pi_V = \{(U, V, W, R) \in \mathbb{R}^4 : U = W = 0\}.$$

The two-dimensional planes Π_U and Π_V can be understood as the spaces in which prey or predators, respectively, are extinct. In particular, the origin $\mathbf{p}_0 \in \Pi_U \cap \Pi_V$. The restriction of (7) to Π_U is given

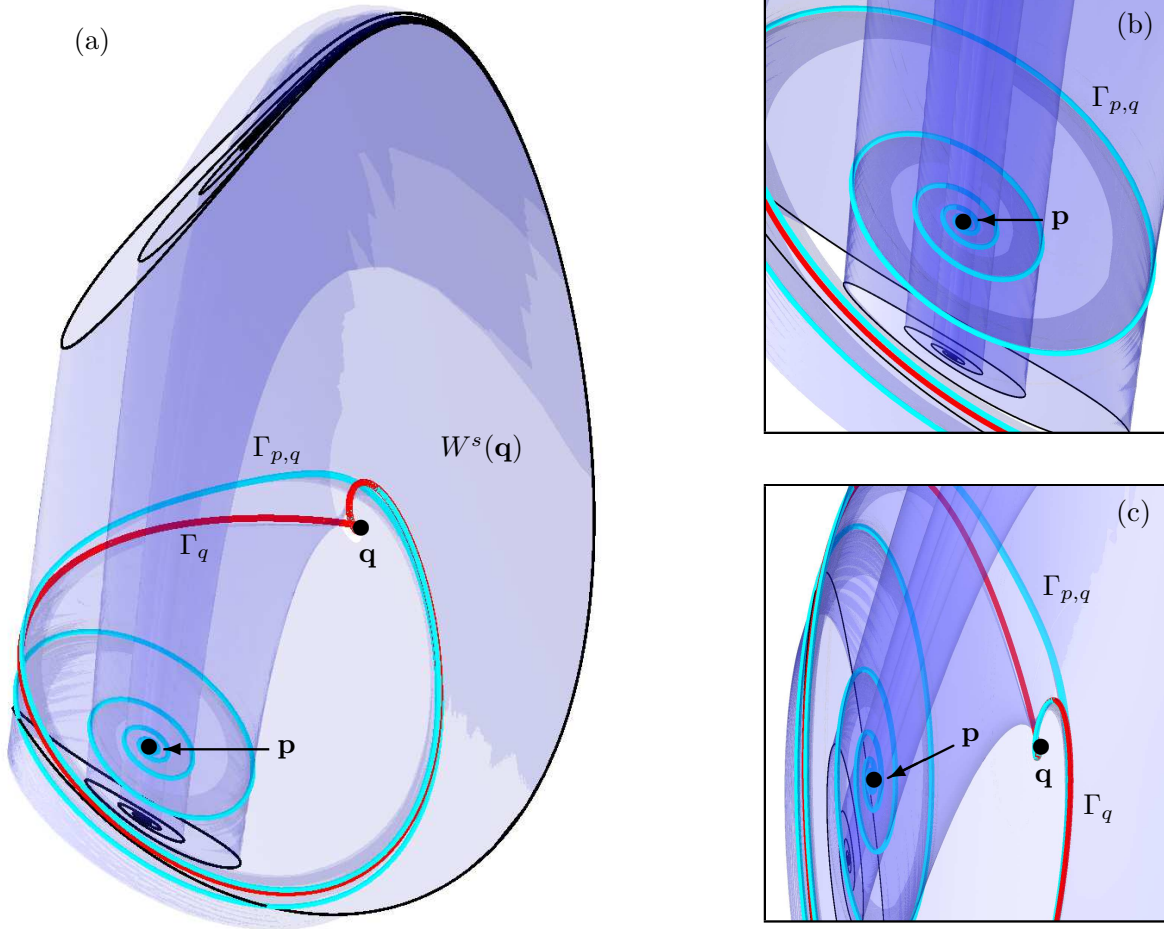


FIGURE 18. The stable manifold $W^s(\mathbf{q})$ of \mathbf{q} projected onto the UVW space in panel (a) when $(m, d) \approx (0.0463358, 1.3080156) \in h_q$. The manifold $W^s(\mathbf{q})$ contains a family of coexisting heteroclinic orbits which join the equilibrium \mathbf{p} to \mathbf{q} as well as the primary focus-focus homoclinic connection Γ_q to \mathbf{q} . One of such heteroclinic orbits is represented by the trajectory $\Gamma_{p,q}$. Panels (b) and (c) show enlargements near the equilibria \mathbf{p} and \mathbf{q} , respectively. The other parameter values are the same as in figure 2.

by

$$X_U : \begin{cases} \frac{dU}{dz} = W, \\ \frac{dW}{dz} = \frac{1}{d} (cW - sU^2(U - m)(1 - U)). \end{cases} \quad (12)$$

System (12) has three equilibria: $\mathbf{0} = (0, 0)$, $(m, 0)$ and $(1, 0)$, which correspond to the restrictions of \mathbf{p}_0 , \mathbf{p}_m and \mathbf{p}_1 , respectively, to Π_U . The equilibrium $(m, 0)$ is a hyperbolic repeller and $(1, 0)$ is a hyperbolic saddle of (12). This result is a direct consequence of Hartman-Grobman theorem. Indeed,

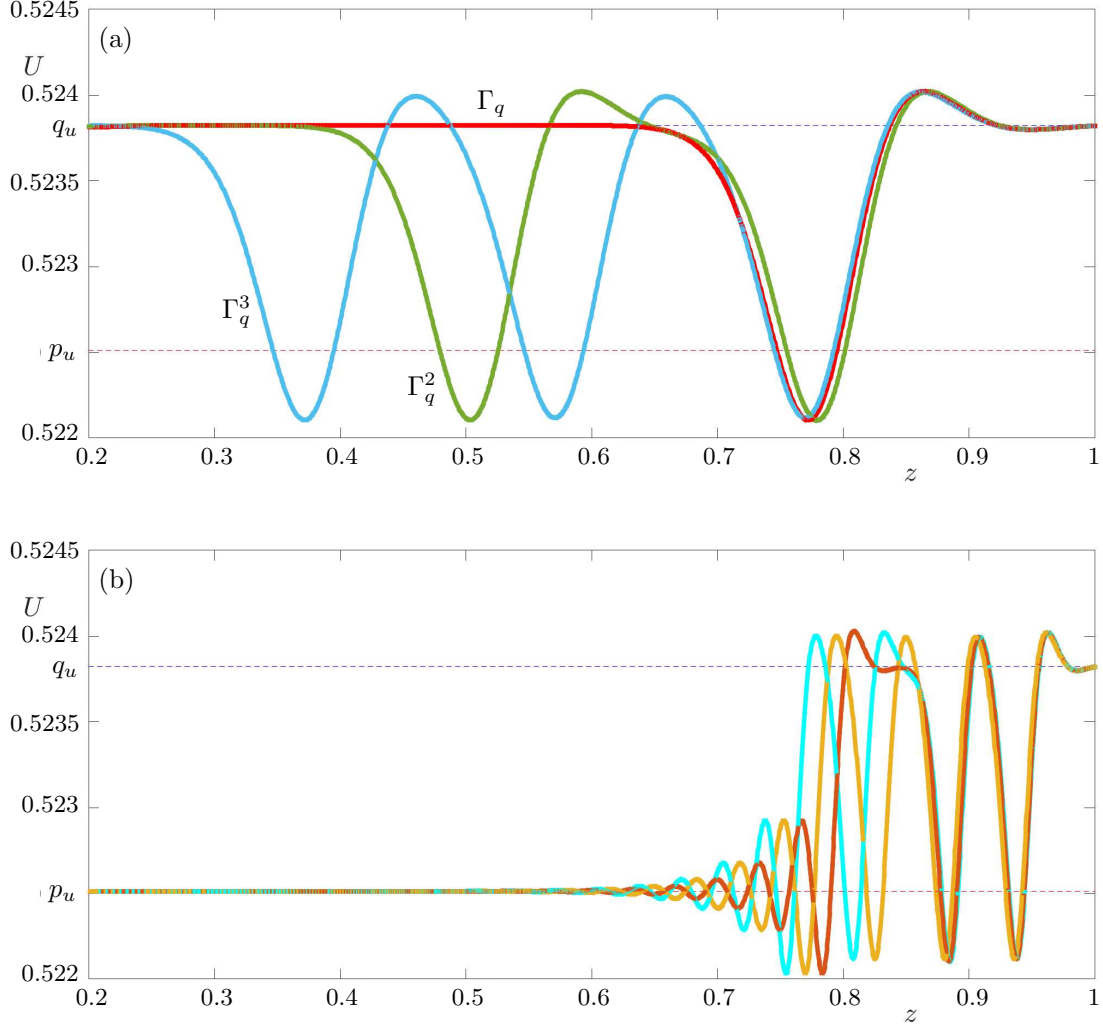


FIGURE 19. Spatial profiles of the prey U associated with the wave pulses Γ_q , Γ_q^2 and Γ_q^3 in panel (a); and three representative traveling fronts $\Gamma_{p,q}^1$, $\Gamma_{p,q}^2$, and $\Gamma_{p,q}^3$ in panel (b), when $(m, d) \approx (0.0463358, 1.3080156) \in h_q$. The other parameter values are the same as in figure 2.

the linear part of (12) is given by

$$DX_U(U, W) = \begin{pmatrix} 0 & 1 \\ \frac{s}{d}(4U^3 - 3(m+1)U^2 + 2mU) & \frac{c}{d} \end{pmatrix}.$$

Therefore, evaluation of DX_U at $(m, 0)$ and $(1, 0)$ is given, respectively, by

$$DX_U(m, 0) = \begin{pmatrix} 0 & 1 \\ \frac{s}{d}m^2(m-1) & \frac{c}{d} \end{pmatrix}, \quad DX_U(1, 0) = \begin{pmatrix} 0 & 1 \\ \frac{s}{d}(1-m) & \frac{c}{d} \end{pmatrix}.$$

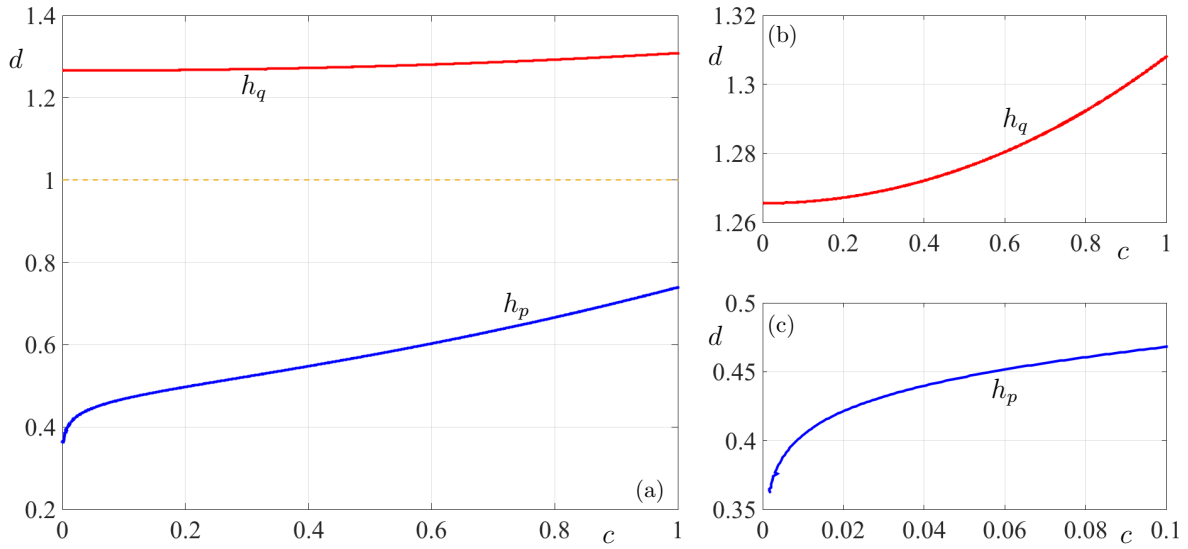


FIGURE 20. The homoclinic bifurcation curves h_p and h_q in the (c, d) -plane in panel (a). Panels (b) and (c) show enlargements near the curves h_q and h_p , respectively (the apparently different shape of each curve is due to the different scales in each plot). Parameter $m = 0.0463358$ and the other parameters are as in figure 2.

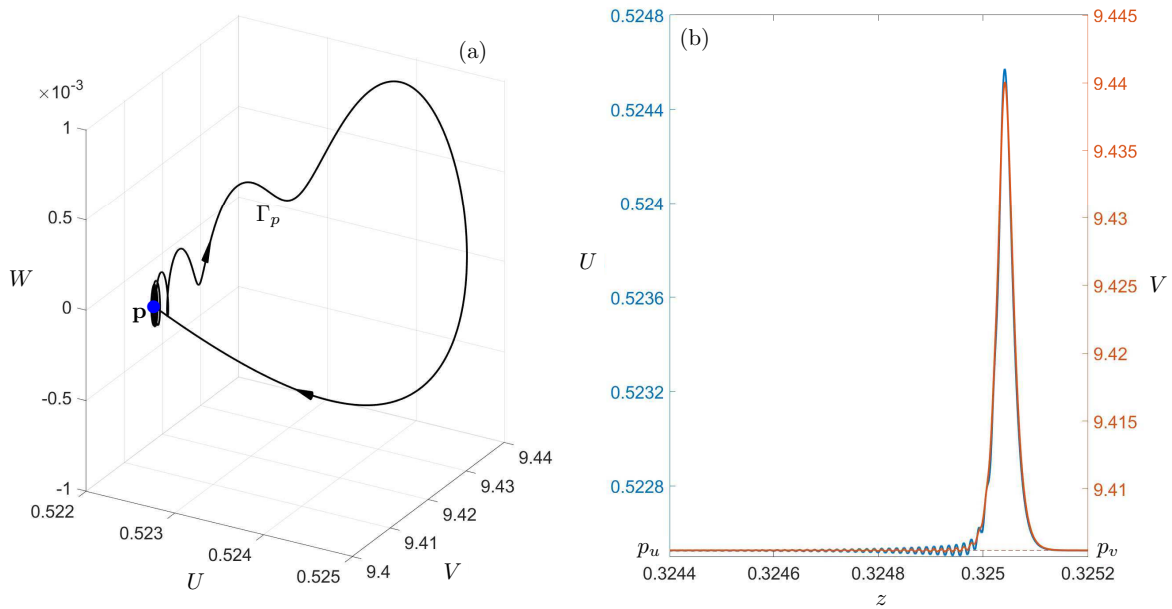


FIGURE 21. The homoclinic orbit Γ_p to \mathbf{p} , when $(c, d) = (0.0479321, 0.4449391)$ in panel (a) and its wave profile in panel (b). The other parameter values are as in figure 20.

Furthermore, the eigenvalues of $DX_U(m, 0)$ and $DX_U(1, 0)$ are given, respectively, by

$$\lambda_{\pm}^m = \frac{c \pm \sqrt{c^2 - 4sdm^2(1-m)}}{2d}, \quad \lambda_{\pm}^1 = \frac{c \pm \sqrt{c^2 + 4sd(1-m)}}{2d}.$$

Since $0 < m < 1$, then we have $c^2 - 4sdm^2(1-m) < c^2$. Therefore, $\text{Re}(\lambda_{\pm}^m) > 0$ and, hence, this proves that $(m, 0)$ is a repeller. On the other hand, let us note that $c^2 + 4sd(1-m) > c^2$, so $\lambda_{-}^1 < 0 < \lambda_{+}^1$. Thus, $(1, 0)$ is a saddle.

In the case of the origin $(0, 0)$ of (12), we have

$$DX_U(\mathbf{0}) = \begin{pmatrix} 0 & 1 \\ 0 & \frac{c}{d} \end{pmatrix},$$

with associated eigenvalues $\lambda_1^0 = 0$, and $\lambda_2^0 = c/d > 0$. Hence, $\mathbf{0}$ is a non-hyperbolic equilibrium. The eigenvectors of $DX_U(\mathbf{0})$ associated with λ_1^0 and λ_2^0 are $v_1^0 = (1, 0)^T$ and $v_2^0 = (c, d)^T$, respectively. According to the Centre Manifold theorem [33], the origin of (12) has a one-dimensional local centre manifold $W_{\text{loc}}^c(\mathbf{0})$ which is tangent to v_1^0 at $\mathbf{0}$. This implies that $W_{\text{loc}}^c(\mathbf{0})$ can be represented locally as the graph of a function $W = W(U)$ that satisfies $W(0) = W'(0) = 0$ (for further details, see [43]). By taking the Taylor series expansion of this function around $U = 0$, we have

$$W(U) = \sum_{k=2}^r a_k U^k + \mathcal{O}(U^{r+1}),$$

where the coefficients $a_k \in \mathbb{R}$, and $\mathcal{O}(U^{r+1})$ are terms of order $r+1$ and higher of the Taylor series of $W(U)$. Here, the coefficients a_k are determined by substitution of $W = W(U)$ into (12). Thus, after some calculations, we obtain

$$W(U) = -\frac{ms}{c}U^2 + \mathcal{O}(U^3).$$

If we restrict (12) to $W_{\text{loc}}^c(\mathbf{0})$, we obtain the one-dimensional differential equation

$$U' = W(U) = -\frac{ms}{c}U^2 + \mathcal{O}(U^3).$$

Then, for $U > 0$ small enough, we have that $U' < 0$. Therefore, $\mathbf{0}$ is a local attractor in $W_{\text{loc}}^c(\mathbf{0})$. Since $\lambda_2^0 > 0$, it follows that $\mathbf{0}$ is a non-hyperbolic saddle point of (12).

Figure 22 shows the phase portrait of (12). The global centre manifold $W^c(\mathbf{0})$ extends itself (for $z < 0$) along the flow of (12) and forms a heteroclinic connection to $(m, 0)$. This corresponds to a wave front in (5) in which—in spite of the predator's absence—the prey population becomes extinct throughout space in the long term. Moreover, since $W^u(m, 0)$ is a two-dimensional unstable manifold, the intersection along $W^c(\mathbf{0}) \cap W^u(m, 0)$ is transversal. It follows that the associated wave front persists under small parameter variations. Furthermore, no other saddle connection occurs in (12). Only under suitable parameter perturbations, the manifolds $W^u(\mathbf{0})$ and $W^s(1, 0)$ may come to intersect along a second heteroclinic orbit from $(0, 0)$ to $(1, 0)$. While finding the right parameter combination for this event to happen is beyond the scope of this paper, we can surely say that such intersection would be non-transversal. Hence, the associated traveling front would not be robust under parameter variation.

Finally, a similar analysis of (7) restricted to the invariant plane Π_V reveals that there are either no homoclinic, heteroclinic orbits nor limit cycles with non-negative V -coordinates in Π_V . Therefore, there are no plausible traveling waves of (5) occurring in the absence of prey population.

11. DISCUSSION

Upon taking into consideration a diffusion process in model (2), we highlight that its dynamical richness considerably raises. Indeed, it made appear the three main types of traveling waves we were looking for: wave pulses, wave fronts, and wave trains. Most of these orbits allow us to conclude that

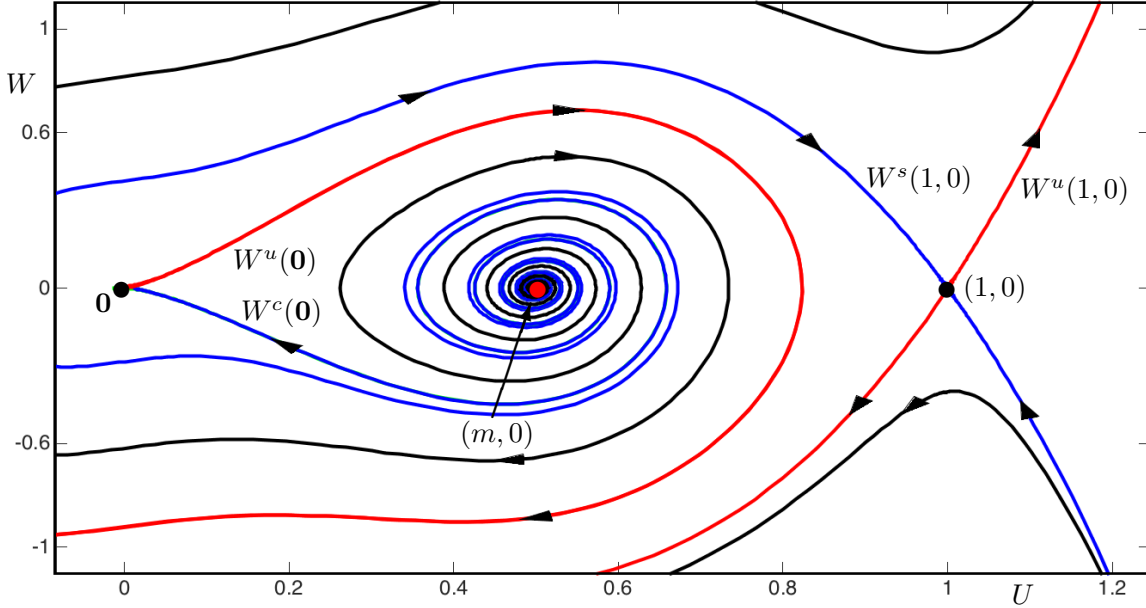


FIGURE 22. The centre manifold $W^c(\mathbf{0})$ extends itself (for $z < 0$) along the flow of (12) and forms a heteroclinic connection to $(m, 0)$. This corresponds to a wave front in (5) in the absence of predators. Parameter values in (12) are $(c, d, m, s) = (1, 2.4, 0.5, 100)$.

there are conditions under which both prey and predator populations may survive in the long term. Furthermore, these showed us that, if both species coexist, then the predator population is always higher where we have a larger prey populace. On the other hand, regarding the analysis made in the invariant planes, we found that there is a wave front (in which predators are absent) that joins two stationary states. In particular, this orbit begins with a spatially homogeneous prey population, which tends to extinction in the long term.

Let us observe that each traveling wave is a stationary solution of system

$$\begin{cases} u_t = du_{zz} - cu_z + su(u - m)(1 - u)(u + v) - auv, \\ v_t = v_{zz} - cv_z + buv - gv(u + v), \end{cases} \quad (13)$$

which coincides with system (5), once the change of variables $(x, t) \rightarrow (x + ct, t)$ has been made. By using this approach, we studied the stability of every shown solution, and we found that each of them is an unstable trajectory. This means that such trajectories will be left in the long term when any perturbation is applied. For further details, see [58].

On the other hand, the presence of chaos in system (7) indicates that setting initial conditions for populations that are well modeled by it in the real world may be unreliable as a consequence of initial condition sensitivity features. In other words, any change in that condition may give rise to an erratic population behavior as time goes by. As can be seen in sections above, key parameters are crucial as well as pivotal theoretical paradigms that should be met to regulate chaotic traits and hence avoid erratic behavior. Therefore, the multiple wave solutions coexisting with chaos emerge as a manifestation of regular spatiotemporal evolution in the midst of such complex behavior. The fact that we are able to pinpoint the specific associated homo/heteroclinic orbits and periodic solutions among chaotic dynamics becomes more relevant in light of these findings.

TABLE 1. Summary of the main traveling wave solutions.

Wave type	Region in (m, d) plane	Orbit in phase space
Type A wave pulse	Bifurcation curve h_q	Focus-focus homoclinic orbit Γ_q
Type B wave pulse	Bifurcation curve h_p	Saddle-focus homoclinic orbit Γ_p
Type C wave pulse	Neighborhoods of h_q	Focus-focus 2-homoclinic orbit Γ_q^2
Type D wave pulse	Neighborhoods of h_p	Saddle-focus 2-homoclinic orbit Γ_p^2
Type E wave pulse	Neighborhoods of h_p	Saddle-focus 4-homoclinic orbit Γ_p^4
Type F wave pulse	Neighborhoods of h_q	Focus-focus 3-homoclinic orbit Γ_q^3
Type A wave front	Region I	Heteroclinic orbit from \mathbf{q} to \mathbf{p} $\Gamma_{q,p}$
Type B wave front	h_q and Regions III, IV, V	Heteroclinic orbit from \mathbf{p} to \mathbf{q} $\Gamma_{p,q}$
Type A wave train	Regions II, III, IV, V and VI	Limit cycle, Γ
Type B wave train	Regions III and V	2-turns limit cycle, Γ^2
Type C wave train	Region III	4-turns limit cycle, Γ^4
Type D wave train	Region III	8-turns limit cycle, Γ^8

Regarding the diffusion process, let us notice that the condition $d > 1$ favors the unpredictability of populations, i.e., system (7) is more likely to be chaotic when the prey diffusivity is higher than that of predators. Contrary to a typical Turing pattern existence analysis as in [9], where $d < 1$ is assumed, our findings show that the greater spreading characteristics of the prey are, the lesser monotony of the predator-prey interaction is observed. In other words, whenever conditions are met in a way that populations coexistence occurs, a distinguished relation between predator-prey transport efficiency and the carrying capacity and mean individual fitness ratio of preys seems to be crucial to prevent uncertain behaviors, which may come from chaotic response. Specifically, we can find chaos when (m, d) belongs to any of the h_p , h_q and NS curves, or some of their neighborhoods; see figure 5 and discussion in section 5.

Finally, table 1 shows a list of all the traveling waves exposed throughout this paper, together with the regions of the bifurcation diagram where they can be found. We highlight that we made this table according to the obtained information, and the mentioned regions may not be the only ones where the given traveling waves can be found.

It is relevant to remember that there are regions where two or more types of traveling waves exist simultaneously. For example, if (m, d) is in the intersection between h_q and h_p , then there are two homoclinic orbits, Γ_q and Γ_p . Furthermore, let us remember that Γ^2 is branched from Γ when (m, d) crosses the PD curve from region II to III. However, Γ does not disappear after this event. In fact, after the successive period doubling bifurcations, a large number of wave trains may be found together in the phase portrait of system (7). Finally, we should recall that when $(m, d) \approx (0.0463358, 1.3080156) \in h_q$, there is a family of heteroclinic orbits, which go from \mathbf{p} to \mathbf{q} . These arise from a transverse intersection between $W^u(\mathbf{p})$ and $W^s(\mathbf{q})$, which indicates that these solutions are robust under small changes of parameter values. This result can be interpreted as follows: for suitable initial conditions and Allee threshold and sensitive diffusion ratio values, traveling fronts mimicking invasion-like traits of both populations are likely able to be observed, and they persist under any sufficiently small perturbation.

A relevant fact regarding the homoclinic orbit Γ_q is that it presents Shilnikov focus-focus homoclinic chaos in a concrete model vector field. Indeed, most of the studies about this bifurcation have been carried out (so far) only theoretically [27, 63]. Moreover, as far as we know, this work represents the first example of the actual computation of a global invariant manifold involved in a focus-focus homoclinic bifurcation in \mathbb{R}^4 .

On the other hand, according to the summary given in table 1, to obtain an oscillatory behavior of populations in space as time goes by, the condition is to be in any of the regions II-VI of the bifurcation diagram. In these, many wave trains with different spatiotemporal periods can be found. Finally, to avoid chaos and ensure that both species establish in a stationary state in which they survive in the long term, then the main requirement for the model parameters is to remain away from the homoclinic bifurcation curves and torus bifurcations.

The amplitude of the oscillations varies in markedly different scales for the rescaled variables, and variations in V are much more pronounced than that of U for pulses, fronts and trains. This difference in amplitudes can be explained by paying attention to the following observations: (i) the prey and the predator populations spatially spread at distinct rates. This rate difference provides that the low-diffusivity population promotes a heterogeneous aggregation of the two populations along the domain; in consequence, both traveling-wave profiles propagate in a spatially non-homogenous shape, regardless of $d < 1$ or $d > 1$; (ii) the prey-predator ratio in the original variables N/P prevails as both amplitudes are of the same order in any scenarios here considered; (iii) upon integrating system (5) along the whole finite spatial domain and assuming uniform convergence in time, we obtain that solutions satisfy formulae:

$$(14a) \quad \int_{-L}^L [su(u-m)(1-u)(u+v) - auv] dx = \frac{d\mathcal{B}_1}{dt},$$

$$(14b) \quad \int_{-L}^L [buw - gv(u+v)] dx = \frac{d\mathcal{B}_2}{dt},$$

where the total biomasses are given by $\mathcal{B}_1(t) = \int_{-L}^L u dx$ and $\mathcal{B}_2(t) = \int_{-L}^L v dx$, regardless of whether the boundary conditions for u_x and v_x vanish or cancel out each other at $x = \pm L$. Moreover, once we define the weighed total biomass by $\mathcal{B}(t) := b\mathcal{B}_1(t) + a\mathcal{B}_2(t)$, from (14), we obtain formula

$$(15) \quad \int_{-L}^L [bsu(u-m)(1-u) - agv](u+v) dx = \frac{d\mathcal{B}}{dt}.$$

Upon taking into account $L \gg 1$, we get traveling-wave solutions of (5), which are characterized by having profiles that keep their shape over time. Now, we consider a moving interval-frame $\mathcal{J} = [-L - ct, L - ct]$, which ‘‘runs alongside’’ the traveling profiles with the same speed $c \geq 0$. In so doing, integral in the left-hand side term of (15) over \mathcal{J} is constant for all $t \geq 0$. That is, since traveling-wave profiles displacement only changes their position in time, the weighed total biomass traveling speed is therefore conserved, i.e. $d\mathcal{B}/dt \equiv \mathcal{C}_0$, where \mathcal{C}_0 is constant. Thus, as $u + v \geq 0$ for all $|x| \leq L$, the total biomasses of the two populations follow a conservation-like property for traveling-wave solutions. Namely, as the wave variable $z = x + ct$ corresponds to a spatial translation for $t \geq 0$, populations amplitudes balance each other to satisfy identity (15) for a constant weighed total biomass rate of change \mathcal{C}_0 .

It is interesting to note that identities in (14) are also satisfied for stationary solutions; that is, upon setting $u_t = v_t = 0$, we have relation (15) with $d\mathcal{B}/dt \equiv 0$, when homogeneous Neumann boundary conditions are in place. Similar identities are obtained for Dirichlet, periodic and mixed-type boundary conditions, as well. Details about stationary solutions of (5) are omitted here, but will appear in a new manuscript based on current research by these authors.

APPENDIX A. TWO-DIMENSIONAL INVARIANT MANIFOLDS AS A FAMILIES OF ORBIT SEGMENTS

The two-dimensional global manifolds in this paper are computed as families of orbit segments, which can be obtained as solutions of a suitable boundary value problem (BVP), irrespective of the vector field undergoing a homoclinic or heteroclinic bifurcation. This allows us to make use of AUTO to implement and solve the BVP; then, the manifold is “built up” by continuation of the respective orbit segments [24, 40, 41]. All images of $W^s(\mathbf{p})$ and $W^{ss}(\mathbf{q})$ are then obtained by rendering the respective portion of the manifold as a surface from the computed orbit segments with dedicated Matlab routines.

In this appendix we focus on the case of a stable manifold (a similar approach can be adopted to compute unstable manifolds by considering unstable eigenvalues and reversing time); see also [3, 1, 7, 54] for further details and applications. We consider a function $\mathbf{u} : [0, 1] \rightarrow \mathbb{R}^4$, that solves the differential equation

$$(16a) \quad \frac{d}{d\tau} \mathbf{u}(\tau) = TF(\mathbf{u}(\tau)),$$

where $F : \mathbb{R}^4 \rightarrow \mathbb{R}^4$ stands for the vector field (7). Let us notice that (16a) is a scaled version of (7) in which the integration time T of an orbit segment appears now as an explicit parameter. In this way, the actual integration time over an orbit segment of (16a) is always 1. The function \mathbf{u} represents a unique orbit segment $\{\mathbf{u}(\tau) \in \mathbb{R}^4 : 0 \leq \tau \leq 1\}$ of (16a) provided suitable boundary conditions are imposed at one or both end points $\mathbf{u}(0)$ and $\mathbf{u}(1)$. (This same approach can be applied to calculate periodic orbits by setting $\mathbf{u}(0) = \mathbf{u}(1)$ and imposing additional suitable integral conditions [24]). In the case of orbits in a stable manifold, these constraints arise naturally from the stable manifold theorem, which states that the stable manifold $W^s(\mathbf{q})$ of an equilibrium \mathbf{q} is tangent to its stable eigenspace $E^s(\mathbf{q})$ at \mathbf{q} [43, 33]. Hence, we can obtain an approximation of $W^s(\mathbf{q})$ as a one-parameter family of orbit segments ending at $E^s(\mathbf{q})$, sufficiently near \mathbf{q} . Formally, this family is parameterised using a suitable sub-manifold of $E^s(\mathbf{q})$. If the eigenvalues of \mathbf{q} are complex conjugate —as is the case of $W^s(\mathbf{q})$ in (7)—, then we consider the boundary conditions given by

$$(16b) \quad \mathbf{u}(1) = \mathbf{w}_0^s + \delta(\mathbf{w}_1^s - \mathbf{w}_0^s) \in \mathbb{R}^4, \quad \delta \in [0, 1),$$

where \mathbf{w}_0^s and \mathbf{w}_1^s are chosen as follows. Let $\mathbf{w}_0^s = \mathbf{q} + \varepsilon \mathbf{v}^s$, where $\varepsilon > 0$ is sufficiently small and $\mathbf{v}^s \in \mathbb{R}^4$ is any non-zero vector in $E^s(\mathbf{q})$. Then, we take \mathbf{w}_1^s as the first return (backwards in time) of the orbit through \mathbf{w}_0^s to the local section generated by \mathbf{v}^s and by any other linearly independent vector that does not belong to $E^s(\mathbf{q})$ [7]. Equation (16b) defines an approximate *fundamental domain*, as each orbit in $W^s(\mathbf{q})$ intersects this segment exactly once. Furthermore, this implies that $\delta \in [0, 1)$ uniquely parameterises a family of orbits $\widehat{W}_{\delta, T}^s(\mathbf{q}) := \{\mathbf{u}_\delta(t) : t \in [0, 1]\}$ that gives an approximation of $W^s(\mathbf{q})$.

The set $\widehat{W}_{\delta, T}^s(\mathbf{q})$ is a (δ, T) -dependent family of orbit segments. Indeed, for each T , we have a one-parameter family of orbit segments that approximates $W^s(\mathbf{q})$. Then, to obtain this approximation in AUTO, we need to specify an initial orbit that satisfies (16a) and (16b), with $\delta = \delta_0 \in [0, 1)$ fixed. To get this trajectory, we consider the trivial orbit $\mathbf{u} \equiv \mathbf{w}_0^s + \delta(\mathbf{w}_1^s - \mathbf{w}_0^s)$ with $T = 0$, and perform a continuation in T until a desired integration time $T = -T^* < 0$, with $\mathbf{u}(1)$ satisfying (16b). Then, a continuation in $\delta \in [0, 1)$ allows us to obtain the desired approximation of $W^s(\mathbf{q})$ as a family of orbit segments for $T = -T^*$ fixed. Moreover, by construction, the family $\widehat{W}_{\delta, T}^s(\mathbf{q})$ lies in an $\mathcal{O}(\varepsilon^2)$ neighbourhood of $W^s(\mathbf{q})$.

Instead of keeping a particular integration time T fixed, it is possible to restrict the point $\mathbf{u}(0)$. This allows us, for instance, to get the intersection $W^s(\mathbf{q}) \cap M$ with a codimension one submanifold $M = \{\mathbf{x} \in \mathbb{R}^4 : G(\mathbf{x}) = 0\}$, by imposing another boundary condition given by

$$(16c) \quad G(\mathbf{u}(0)) = 0.$$

Solutions of (16a) with boundary conditions (16b) and (16c) are orbits that begin at M and end at the approximate fundamental domain of $W^s(\mathbf{q})$ near \mathbf{q} .

To obtain a first trajectory in this case, we continue an orbit that satisfies (16b) for $\delta = \delta_0 \in [0, 1)$ fixed, while we monitor the value of $G(\mathbf{u}(0))$. We stop this continuation when condition (16c) is satisfied. This starting orbit segment can then be continued as a one-parameter family of solutions of the boundary value problem (16) in the free parameters δ and T , so that the point $\mathbf{u}(0)$ traces out a one-dimensional curve on M . The two-dimensional manifolds in figures 15, 16, 17 and 18 were obtained by setting M to be the sphere $S_r = \{\mathbf{x} \in \mathbb{R}^4 : \|\mathbf{x} - \mathbf{q}\| = r\}$ with radius $r = 0.03$, centered at \mathbf{q} , where $\|\cdot\|$ denotes the Euclidean norm in \mathbb{R}^4 . We highlight that not every orbit ending at the fundamental domain may intersect M . Also, the intersection set $W^s(\mathbf{q}) \cap M$ could consist of many different curves. In that case, it is necessary to repeat the same procedure for different values of $\delta_0 \in [0, 1)$ to get the whole set. See [7, 40] for further details.

In particular, if $W^s(\mathbf{q})$ contains a heteroclinic orbit flowing from \mathbf{p} to \mathbf{q} , such trajectory is approximated by a bounded orbit segment in the family $\widehat{W}_{\delta, T}^s(\mathbf{q})$ passing sufficiently close to \mathbf{p} . Indeed, if a heteroclinic orbit exists, the two-parameter continuation procedure effectively stops as the integration time diverges. In practice, an approximation of such connecting orbit is obtained at some specific $\delta = \delta^* \in [0, 1)$ with a large integration time $T = -T^*$. A similar criterium can be used to detect secondary n -homoclinic orbits to \mathbf{q} as orbit segments ending near \mathbf{q} as the integration time T diverges. For instance, in figures 18 and 19, the fundamental domain $\delta \in [0, 1)$ is divided into 13 sub-segments by the values $0 < \delta_1 < \delta_2 < \dots < \delta_{12} < 1$. The heteroclinic connections correspond to $\delta_1 \approx 0.317181$, $\delta_2 \approx 0.317265$, $\delta_6 \approx 0.319579$, $\delta_8 \approx 0.319621$, $\delta_9 \approx 0.319904$, $\delta_{11} \approx 0.319917$ and $\delta_{12} \approx 0.331911$. On the other hand, we have the primary homoclinic orbit at $\delta_7 \approx 0.319616$, and four secondary homoclinic orbits at $\delta_3 \approx 0.317284$, $\delta_4 \approx 0.317285$, $\delta_5 \approx 0.317285$ and $\delta_{10} \approx 0.319906$.

CONFLICT OF INTEREST

The authors declare that they have no conflict of interest.

REFERENCES

1. P. Aguirre, E. Doedel, B. Krauskopf, and H. M. Osinga, *Investigating the consequences of global bifurcations for two-dimensional invariant manifolds of vector fields*, *Discr. Cont. Dynam. Syst.* **29** (2010), no. 4, 1309–1344.
2. P. Aguirre, B. Krauskopf, and H. M. Osinga, *Global invariant manifolds near homoclinic orbits to a real saddle:(non) orientability and flip bifurcation*, *SIAM J. Appl. Dynam. Syst.* **12** (2013), no. 4, 1803–1846.
3. Pablo Aguirre, *Bifurcations of two-dimensional global invariant manifolds near a noncentral saddle-node homoclinic orbit*, *SIAM Journal on Applied Dynamical Systems* **14** (2015), no. 3, 1600–1643.
4. Pablo Aguirre, José D Flores, and Eduardo González-Olivares, *Bifurcations and global dynamics in a predator–prey model with a strong allee effect on the prey, and a ratio-dependent functional response*, *Nonlinear Analysis: Real World Applications* **16** (2014), 235–249.
5. Pablo Aguirre, Eduardo González-Olivares, and Eduardo Sáez, *Three limit cycles in a leslie–gower predator–prey model with additive allee effect*, *SIAM Journal on Applied Mathematics* **69** (2009), no. 5, 1244–1262.
6. ———, *Two limit cycles in a leslie–gower predator–prey model with additive allee effect*, *Nonlinear Analysis: Real World Applications* **10** (2009), no. 3, 1401–1416.
7. Pablo Aguirre, Bernd Krauskopf, and Hinke M Osinga, *Global invariant manifolds near a shilnikov homoclinic bifurcation*, *Journal of Computational Dynamics* **1** (2014), no. 1, 1–38.
8. H Resit Akcakaya, Roger Arditi, and Lev R Ginzburg, *Ratio-dependent predation: an abstraction that works*, *Ecology* **76** (1995), no. 3, 995–1004.
9. S. Aly, I. Kim, and D. Sheen, *Turing instability for a ratio-dependent predator-prey model with diffusion*, *Applied Mathematics and Computation* **217** (2011), no. 17, 7265–7281.
10. Roger Arditi and Lev R Ginzburg, *Coupling in predator-prey dynamics: ratio-dependence.*, *Journal of theoretical biology* **139** (1989), no. 3, 311–326.
11. Roger Arditi and Henni Saiah, *Empirical evidence of the role of heterogeneity in ratio-dependent consumption*, *Ecology* **73** (1992), no. 5, 1544–1551.
12. Nicolas Bacaër, *A short history of mathematical population dynamics*, Springer Science & Business Media, 2011.

13. L. A. Belyakov, *Bifurcation of systems with homoclinic curve of a saddle-focus with saddle quantity zero*, Mat. Zam. **36** (1984), 681–689.
14. A. Berryman, A. Gutierrez, and R. Arditi, *Credible, parsimonious and useful predator-prey models: A reply to Abrams, Gleeson, and Sarnelle*, Ecology **76** (1995), 1980–1985.
15. Víctor Breña-Medina and Alan Champneys, *Subcritical Turing bifurcation and the morphogenesis of localized patterns*, Physical Review E **90** (2014), no. 3, 032923.
16. Alan R Champneys, Yu A Kuznetsov, and Björn Sandstede, *A numerical toolbox for homoclinic bifurcation analysis*, International Journal of Bifurcation and Chaos **6** (1996), no. 05, 867–887.
17. E.A. Colding, M.J. P Lank, and SS. Benhamou, *Random walk models in biology*, J. R. Soc. Interface **5** (2008), no. 25, 813–834.
18. Dana Contreras Julio and Pablo Aguirre, *Allee thresholds and basins of attraction in a predation model with double allee effect*, Mathematical Methods in the Applied Sciences **41** (2018), no. 7, 2699–2714.
19. Dana Contreras-Julio, Pablo Aguirre, José Mujica, and Olga Vasilieva, *Finding strategies to regulate propagation and containment of dengue via invariant manifold analysis*, SIAM Journal on Applied Dynamical Systems **19** (2020), no. 2, 1392–1437.
20. Franck Courchamp, Ludek Berec, and Joanna Gascoigne, *Allee effects in ecology and conservation*, Oxford University Press, 2008.
21. Franck Courchamp, Tim Clutton-Brock, and Bryan Grenfell, *Inverse density dependence and the allee effect*, Trends in ecology & evolution **14** (1999), no. 10, 405–410.
22. JHP Dawes and MO Souza, *A derivation of holling's type i, ii and iii functional responses in predator-prey systems*, Journal of theoretical biology **327** (2013), 11–22.
23. A. Dhooge, W. Govaerts, Yu. A. Kuznetsov, H. G.E. Meijer, and B. Sautois, *New features of the software matcont for bifurcation analysis of dynamical systems*, Mathematical and Computer Modelling of Dynamical Systems **14** (2008), no. 2, 147–175.
24. E. J. Doedel, *Lecture notes on numerical analysis of nonlinear equations*, Numerical Continuation Methods for Dynamical Systems, Springer, 2007, pp. 1–49.
25. Eusebius J Doedel, Thomas F Fairgrieve, Björn Sandstede, Alan R Champneys, Yuri A Kuznetsov, and Xianjun Wang, *Auto-07p: Continuation and bifurcation software for ordinary differential equations*, 2007.
26. N. Fenichel, *Geometric singular perturbation theory for ordinary differential equations*, J. Differ. Equations **31** (1979), no. 1, 53–98.
27. AC Fowler and CT Sparrow, *Bifocal homoclinic orbits in four dimensions*, Nonlinearity **4** (1991), no. 4, 1159–1182.
28. Joanna C Gascoigne and Romuald N Lipcius, *Allee effects driven by predation*, Journal of Applied Ecology **41** (2004), no. 5, 801–810.
29. Eduardo González-Olivares, Betsabé González-Yañez, Jaime Mena-Lorca, and José D Flores, *Uniqueness of limit cycles and multiple attractors in a gause-type predator-prey model with nonmonotonic functional response and allee effect on prey*, Mathematical Biosciences and Engineering **10** (2013), 345–367.
30. Stephen D Gregory and Franck Courchamp, *Safety in numbers: extinction arising from predator-driven allee effects*, Journal of animal ecology **79** (2010), no. 3, 511–514.
31. Xiaona Guan, Weiming Wang, and Yongli Cai, *Spatiotemporal dynamics of a leslie-gower predator-prey model incorporating a prey refuge*, Nonlinear Analysis: Real World Applications **12** (2011), no. 4, 2385–2395.
32. J. Guckenheimer, B. Krauskopf, H. M. Osinga, and B. Sandstede, *Invariant manifolds and global bifurcations*, Chaos **25** (2015), no. 9, 097604.
33. John Guckenheimer and Philip Holmes, *Nonlinear oscillations, dynamical systems, and bifurcations of vector fields*, vol. 42, Springer Science & Business Media, 2013.
34. AP Gutierrez, *Physiological basis of ratio-dependent predator-prey theory: the metabolic pool model as a paradigm*, Ecology **73** (1992), no. 5, 1552–1563.
35. Morris W. Hirsch, *Differential topology*, Graduate Texts in Mathematics, vol. 33, Springer, 1976.
36. Crawford S Holling, *The components of predation as revealed by a study of small-mammal predation of the european pine sawfly*, The Canadian Entomologist **91** (1959), no. 5, 293–320.
37. ———, *Some characteristics of simple types of predation and parasitism*, The Canadian Entomologist **91** (1959), no. 7, 385–398.
38. Ale Jan Homburg and Björn Sandstede, *Homoclinic and heteroclinic bifurcations in vector fields*, Handbook of Dynamical Systems **3** (2010), 379–524.
39. B. Krauskopf and T. Rieß, *A Lin's method approach to finding and continuing heteroclinic connections involving periodic orbits*, Nonlinearity **21** (2008), no. 8, 1655.
40. Bernd Krauskopf and Hinke M Osinga, *Computing invariant manifolds via the continuation of orbit segments*, Numerical Continuation Methods for Dynamical Systems, Springer, 2007, pp. 117–154.

41. Bernd Krauskopf, Hinke M Osinga, Eusebius J Doedel, Michael E Henderson, John Guckenheimer, Alexander Vladimirov, Michael Dellnitz, and Oliver Junge, *A survey of methods for computing (un) stable manifolds of vector fields*, Modeling And Computations In Dynamical Systems: In Commemoration of the 100th Anniversary of the Birth of John von Neumann, World Scientific, 2006, pp. 67–95.
42. Yang Kuang and Edoardo Beretta, *Global qualitative analysis of a ratio-dependent predator-prey system*, Journal of mathematical biology **36** (1998), no. 4, 389–406.
43. Yuri A Kuznetsov, *Elements of applied bifurcation theory*, vol. 112, Springer Science & Business Media, 2013.
44. M. Lewis and P.Kareiva, *Allee dynamics and the spread of invading organisms*, Theo. Popul. Biol. **43** (1993), 141–158.
45. M.A. Lewis and B. Li, *Spreading Speed, Traveling Waves, and Minimal Domain Size in Impulsive Reaction-Diffusion Models*, Bull. Math. Biol. **74** (2012), 2383–2402.
46. Huiru Li and Haibin Xiao, *Traveling wave solutions for diffusive predator-prey type systems with nonlinear density dependence*, Computers & mathematics with applications **74** (2017), no. 10, 2221–2230.
47. Xiaobiao Lin, Peixuan Weng, and Chufen Wu, *Traveling wave solutions for a predator-prey system with sigmoidal response function*, Journal of Dynamics and Differential Equations **23** (2011), no. 4, 903–921.
48. Robert F Luck, *Evaluation of natural enemies for biological control: a behavioral approach*, Trends in Ecology & Evolution **5** (1990), no. 6, 196–199.
49. Dolnik M., Zhabotinsky A.M., A.B. Rovinsky, and Epstein I.R., *Spatio-temporal patterns in a reaction-diffusion system with wave instability*, Chem. Eng. Sci. **55** (2000), 223–231.
50. James D Murray, *Mathematical biology ii: Spatial models and biomedical applications*, vol. 18, Springer, 2001.
51. ———, *Mathematical biology: I. an introduction*, vol. 17, Springer Science & Business Media, 2007.
52. E. Nelson, *Dynamical Theories of Brownian Motion*, Princeton University Press, 2976.
53. A. Okubo and S.A. Levin, *Diffusion and Ecological Problems: Modern Perspectives*, 2nd ed., Springer, New York, NY, 2000.
54. Hinke M Osinga, *Two-dimensional invariant manifolds in four-dimensional dynamical systems*, Computers & Graphics **29** (2005), no. 2, 289–297.
55. IM Ovsvyannikov and LP Shil'nikov, *Systems with a homoclinic curve of multidimensional saddle-focus type, and spiral chaos*, Mathematics of the USSR-Sbornik **73** (1992), no. 2, 415–443.
56. Lijuan Qin, Feng Zhang, Wanxiong Wang, and Weixin Song, *Interaction between allee effects caused by organism-environment feedback and by other ecological mechanisms*, PloS one **12** (2017), no. 3.
57. Michael L Rosenzweig, *Paradox of enrichment: destabilization of exploitation ecosystems in ecological time*, Science **171** (1971), no. 3969, 385–387.
58. Björn Sandstede, *Stability of travelling waves*, Handbook of dynamical systems, vol. 2, Elsevier, 2002, pp. 983–1055.
59. Jonathan A Sherratt and Matthew J Smith, *Periodic travelling waves in cyclic populations: field studies and reaction-diffusion models*, Journal of the Royal Society Interface **5** (2008), no. 22, 483–505.
60. L. T. Takahashi, N. A. Maidana, W. C. Ferreira, P. Pulino, and H. M. Yang, *Mathematical models for the Aedes aegypti dispersal dynamics: travelling waves by wing and wind*, Bull. Math. Biol. **67** (2005), no. 3, 509–528.
61. Peter Turchin, *Complex population dynamics: a theoretical/empirical synthesis*, Princeton university press, 2003.
62. Vito Volterra, *Variazioni e fluttuazioni del numero d'individui in specie animali conviventi*, C. Ferrari, 1927.
63. Stephen Wiggins, *Global bifurcations and chaos: analytical methods*, vol. 73, Springer Science & Business Media, 2013.
64. GSK Wolkowicz, *Bifurcation analysis of a predator-prey system involving group defence*, SIAM Journal on Applied Mathematics **48** (1988), no. 3, 592–606.
65. Xiujuan Wu, Yong Luo, and Yizheng Hu, *Traveling waves in a diffusive predator-prey model incorporating a prey refuge*, Abstract and Applied Analysis, vol. 2014, Hindawi, 2014.
66. Dongmei Xiao and Shigui Ruan, *Codimension two bifurcations in a predator-prey system with group defense*, International Journal of Bifurcation and Chaos **11** (2001), no. 08, 2123–2131.
67. W. M. S Yamashita, L. T. Takahashi, and G. Chapiro, *Traveling wave solutions for the dispersive models describing population dynamics of Aedes aegypti*, Math. Comput. Simulat. **146** (2018), 90–99.

*DEPARTAMENTO DE MATEMÁTICA, UNIVERSIDAD TÉCNICA FEDERICO SANTA MARÍA, CASILLA 110-V, VALPARAÍSO, CHILE.

E-mail address: edgardo.villar.13@sansano.usm.cl, pablo.aguirre@usm.cl

†DEPARTMENT OF MATHEMATICS, ITAM, RÍO HONDO 1, CIUDAD DE MÉXICO 01080, MÉXICO.

E-mail address: victor.brena@itam.mx